Giuseppe Pontillo

Magnetic Resonance Imaging and Machine Learning for Brain Disorders 2022 - XXXV

Magnetic resonance imaging (MRI) represents a uniquely powerful tool for clinical and basic neuroscience, providing an invaluable window into the in vivo brain.

In recent years, different MRI modalities have found their stable place in the clinical and/or research setting, leading to an ever-increasing number of brain imaging studies.

In this context, machine learning has emerged as a powerful technique for recognizing patterns on high-dimensional MRI datasets.

I present four different case studies in which brain MRI and statistical/machine learning methods are applied in different clinical populations to address specific research questions, including:

(i) modelling brain MRI data using unsupervised machine learning to stratify patients with multiple sclerosis; (ii) building a model of healthy aging using deep learning and brain MRIs and testing whether patients with Fabry disease have older appearing brains compared to healthy subjects; (iii) analyzing MRI-based connectivity to study alterations of brain structural and functional networks in schizophrenia; (iv) using quantitative MRI to characterize brain iron and myelin changes in multiple sclerosis.

UNIVERSITÀ DEGLI STUDI DI NAPOLI FEDERICO II

ICTH PhD

MAGNETIC RESONANCE IMAGING AND MACHINE LEARNING FOR BRAIN DISORDERS

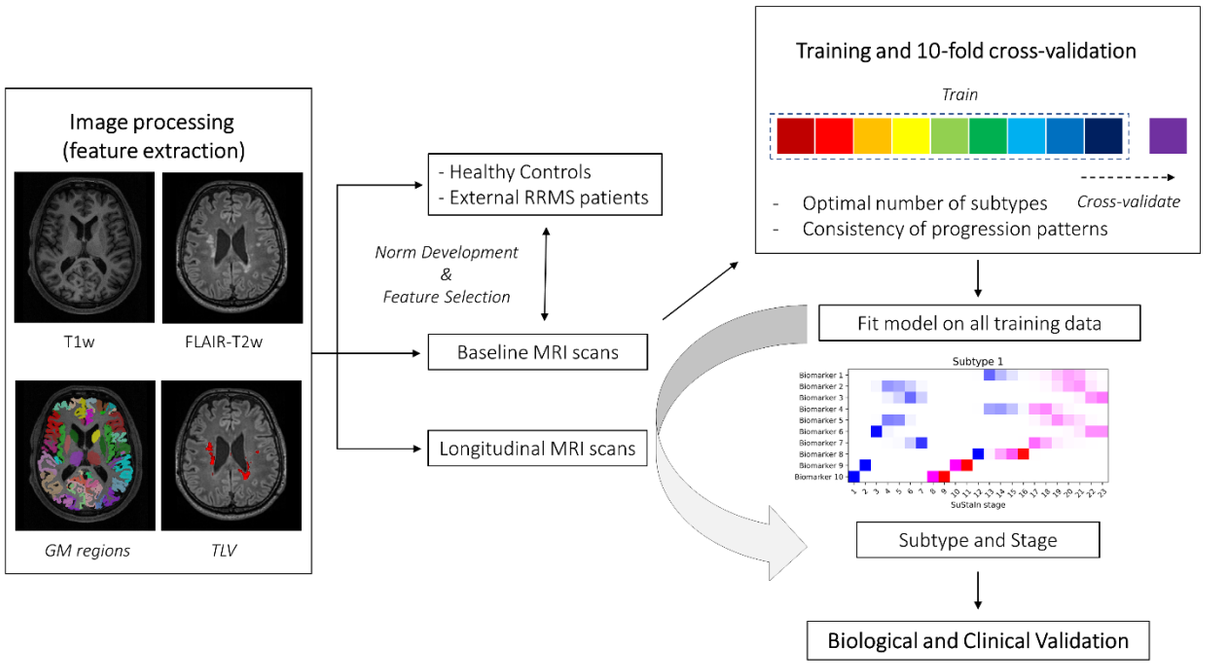

GIUSEPPE PONTILLO

PH.D. IN INFORMATION AND COMMUNICATION TECHNOLOGY FOR HEALTH

UNIVERSITÀ DEGLI STUDI DI NAPOLI
FEDERICO II

Università degli Studi di Napoli Federico II
Ph.D. Program in
Information and Communication Technology for Health
XXXV Cycle

Thesis for the Degree of Doctor of Philosophy

Magnetic resonance imaging and machine learning for brain disorders

by
Giuseppe Pontillo

Advisor: Prof. Daniele Riccio

Co-advisor: Prof. Arturo Brunetti

Scuola Politecnica e delle Scienze di Base
Dipartimento di Ingegneria Elettrica e delle Tecnologie dell'Informazione

To Daria

Fall in love with some activity, and do it! Nobody ever figures out what life is all about, and it doesn't matter. Explore the world. Nearly everything is really interesting if you go into it deeply enough.

— Richard P. Feynman

AVGVST FRIDERICVS IMPERATOR ROMANORVM SEMP

Magnetic resonance imaging and machine learning for brain disorders

Ph.D. Thesis presented
for the fulfillment of the Degree of Doctor of Philosophy in
Information and Communication Technology for Health
by

Giuseppe Pontillo

October 2022

Approved as to style and content by

_____

Prof. Daniele Riccio, Advisor

_____

Prof. Arturo Brunetti, Co-advisor

Università degli Studi di Napoli Federico II
Ph.D. Program in Information and Communication Technology for Health
XXXV cycle - Chairman: Prof. Daniele Riccio
http://icth.dieti.unina.it

Candidate's declaration

I hereby declare that this thesis submitted to obtain the academic degree of Philosophiæ Doctor (Ph.D.) in Information and Communication Technology for Health is my own unaided work, that I have not used other than the sources indicated, and that all direct and indirect sources are acknowledged as references.
Parts of this dissertation have been published in international journals and/or conference articles (see list of the author's publications at the end of the thesis).

Napoli, October 31, 2022

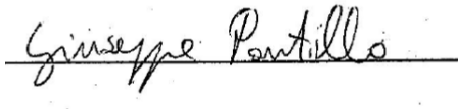

Giuseppe Pontillo

Contents

Abstract

Magnetic resonance imaging (MRI) represents a uniquely powerful tool for clinical and basic neuroscience, providing an invaluable window into the in vivo brain.

In recent years, different MRI modalities have found their stable place in the clinical and/or research setting, leading to an ever-increasing number of brain imaging studies.

In this context, machine learning has emerged as a powerful technique for recognizing patterns on high-dimensional MRI datasets.

I present four different case studies in which brain MRI and statistical/machine learning methods are applied in different clinical populations to address specific research questions, including: (i) modelling brain MRI data using unsupervised machine learning to stratify patients with multiple sclerosis; (ii) building a model of healthy aging using deep learning and brain MRIs and testing whether patients with Fabry disease have older appearing brains compared to healthy subjects; (iii) analyzing MRI-based connectivity to study alterations of brain structural and functional networks in schizophrenia; (iv) using quantitative MRI to characterize brain iron and myelin changes in multiple sclerosis.

Keywords: magnetic resonance imaging, machine learning, brain, multiple sclerosis, Fabry disease, schizophrenia.

Sintesi in lingua italiana

L'imaging di risonanza magnetica (RM) rappresenta uno strumento fondamentale per le neuroscienze cliniche e di base, permettendo di "guardare" all'interno dell'encefalo in vivo in maniera non invasiva.
Negli ultimi anni, diverse modalità di RM hanno trovato un ruolo stabile in ambito clinico e/o di ricerca, portando ad un numero sempre crescente di studi basati su imaging dell'encefalo.
In questo contesto, il machine learning è emerso come uno strumento straordinariamente potente per modellare grandi collezioni di dati RM.
Presento qui quattro diversi esempi di come RM dell'encefalo e metodi statistici/di machine learning possano essere applicati in popolazioni cliniche per rispondere a specifici quesiti di ricerca, che includono: (i) modellare dati di RM dell'encefalo utilizzando machine learning non supervisionato per stratificare pazienti con sclerosi multipla; (ii) costruire un modello di invecchiamento fisiologico utilizzando deep learning e RM dell'encefalo e testare se la malattia di Fabry incide sull'invecchiamento encefalico; (iii) analizzare dati RM di connettività cerebrale per studiare le alterazioni dei network strutturali e funzionali in soggetti con schizofrenia; (iv) utilizzare l'RM quantitativa per caratterizzare le alterazioni di ferro e mielina encefalici associati alla sclerosi multipla.

Parole chiave: risonanza magnetica, machine learning, encefalo, sclerosi multipla, malattia di Fabry, schizofrenia.

Acknowledgements

Part of the author's work has been carried out within the framework of the ECTRIMS-MAGNIMS 2020 and ESNR 2021 Research Fellowship Programs.

List of Acronyms

The following acronyms are used throughout the thesis.

CSF	CerebroSpinal Fluid
CV	Cross-Validation
DGM	Deep Gray Matter
dMRI	diffusion MRI
EDSS	Expanded Disability Status Scale
FC	Funtional Connectivity
FD	Fabry Disease
fMRI	functional MRI
GM	Gray Matter
HS	Healthy Subjects
ML	Machine Learning
MRI	Magnetic Resonance Imaging
MS	Multiple Sclerosis
qMRI	quantitative MRI
RR	Relapsing-Remitting
RS	Resting-State
sMRI	structural MRI
SC	Structural Connectivity
SDMT	Symbol Digit Modalities Test
SZ	Schizophrenia
TLV	Total Lesion Volume
T2-LL	T2-Lesion Load
VBM	Voxel Based Morphometry
VBQ	Voxel Based Quantification
WBV	Whole Brain Volume
WM	White Matter

Chapter

Introduction

Magnetic resonance imaging (MRI) represents a uniquely powerful tool for clinical and basic neuroscience, providing an invaluable window into the in vivo brain.

MRI is intrinsically multiparametric, with different modalities that can be used to highlight different aspects of the brain's structure and function.

Structural MRI (sMRI) is typically used to show the gross anatomy of the brain: that is, mainly gray matter (GM), white matter (WM) and cerebrospinal fluid (CSF). Many varieties of structural imaging exist, each of which can highlight different aspects of brain anatomy, including pathological tissue. T1-weighted images are the most common structural images, used for getting good CNR (contrast-to-noise ratio) and tissue discrimination, especially in healthy subjects (HS).

Diffusion MRI (dMRI) provides indirect information about local physical diffusion processes and axonal fiber directions. It can be used to examine the "wiring" of the brain (i.e., anatomical connectivity), as well as to investigate tissue microstructure.

Functional MRI (fMRI) highlights dynamic changes in the brain in order to examine neuronal function. It provides a surrogate measure of neuronal activity by using the blood oxygenation level dependent (BOLD) effect, which is sensitive to changes of blood oxygenation in response to neuronal firing.

Quantitative MRI (qMRI) goes beyond conventional MRI, which aims primarily at local image contrast, providing quantitative measurements of

specific physical parameters related to the nuclear spin of protons in water. These parameters carry information about the local microstructural environment of the protons (e.g., myelin), and can be used to directly characterize biological tissue microstructure.[1]

In recent years, all these modalities have found their stable place in the clinical and/or research setting. Indeed, the maturation of in vivo neuroimaging has led to incredible quantities of digital information about the human brain. An increasing number of brain imaging studies have started to join the ranks of "big data" science, prompting the usage of novel image analysis and statistical methods for the investigation of high-dimensional MRI datasets.

In particular, machine learning (ML) has emerged as a powerful technique for recognizing patterns on medical images, driven also by the substantial increase in computational performance and the introduction of new algorithms.[2]

Here, I will describe four different case studies in which brain MRI and statistical methods are applied in different clinical populations to address specific research questions.

In Chapter 2, we will see how the unsupervised machine learning modelling of brain MRI data can be used to obtain a biologically and clinically meaningful stratification of patients with multiple sclerosis (MS).

In Chapter 3, we will use deep learning to build a model of healthy aging from brain MRIs and test whether patients with Fabry disease (FD) have older appearing brains compared to HS.

In Chapter 4, we will assess the impact of schizophrenia (SZ) on structural and functional MRI-based brain connectivity.

In Chapter 5, we will use qMRI to characterize MS-related changes of brain iron and myelin and explore their clinical correlates.

Chapter 2

Disease Modelling in Multiple Sclerosis

2.1 Background and Rationale

Brain MRI abnormalities in MS represent objective indicators of the patient's biological status, reflecting pathogenetic mechanisms underlying disease evolution.[3]

Although a massive body of evidence regarding the biological and clinical relevance of MRI biomarkers has been provided through the years by large-N research studies, their implementation in the single-subject setting and therefore in clinical practice remains challenging.[4] Actually, MRI biomarkers exhibit high variance, resulting from both non disease-related confounders (e.g. age, sex, other coexisting physiologic and pathologic conditions) and disease-related phenotypic and temporal heterogeneity, thus hampering the definition of absolute cut-points and limiting their utility for effective patient stratification.

Over the years, technical advances and the emergence of imaging guidelines[5,6] have led to the widespread availability of high-quality clinical MRI scans, including sequences with isotropic voxel resolution suitable for volumetric quantifications.[7] Unfortunately, this goldmine of information remains largely unexploited due to the complexity of meaningfully modelling high-dimensional dataset and the frequent lack of associated data reliably reflecting the patients' clinical status.

Unsupervised ML techniques modelling disease progression based solely

on objective biomarker changes, without reliance on a priori clinical information or explicit biomarker thresholds, represent a valuable approach to overcome these issues.[8] Recently, such methods have been applied to primary neurodegenerative disorders of the Central Nervous System[8,9] and showed promising results when translated into the MS scenario with the aim to characterize the disease-specific sequence of clinical and MRI changes[10,11] or to provide an MRI-driven definition of disease phenotypes.[12]

Based on these premises, we applied a recently developed algorithm called Subtype and Staging Inference (SuStaIn), which identifies data-driven subtypes characterized by distinct trajectories of biomarkers abnormality accumulation, to clinical MRI scans of a large single-center cohort of relapsing-remitting MS (RRMS) patients. We aimed to demonstrate that, based on a fine-grained volumetric mapping of different brain areas and MS lesions obtained from cross-sectional MRI visits, such approach would provide an accurate patient stratification which is both biologically reliable and prognostically meaningful in the light of longitudinal MRIs and long-term (10-year) motor and cognitive evaluations.

2.2 Materials and Methods

2.2.1 Participants

In this monocentric retrospective study, brain MRI studies of patients with an MS diagnosis revised according to the 2010 McDonald criteria[13] and a relapsing-remitting (RR) course[14] were screened for eligibility from the radiological and clinical research databases of the MS center of the University of Naples "Federico II", containing data collected starting from October 2006.

Brain MRI scans of HS from the same databases and an external population of RRMS patients from the University of Genoa were also

selected to develop norms for z-scores calculation and select MRI features. The study was conducted in compliance with the ethical standards and approved by the Ethics Committee "Carlo Romano" of the Host Institution.

2.2.2 Clinical evaluation

For all patients, clinical disability within one week from MRI was estimated using the Expanded Disability Status Scale (EDSS). Patients for whom a long-term clinical and neuropsychological evaluation was available were classified at follow-up (10±2years from baseline MRI) according to: (i) motor disability, ranging from 0 to 3 according to ambulation benchmarks corresponding to EDSS scores <4.0, ≥4.0 and <6.0, ≥6.0 and <7.0, ≥7.0;[15] (ii) cognitive disability, ranging from 0 to 3 and corresponding to the number of impaired (below 1.5 SD age-, sex- and education-corrected normative values in the healthy population)[16] tests at the Brief International Cognitive Assessment of Multiple Sclerosis (BICAMS) battery;[17] (iii) transition to secondary progressive course.[14]

2.2.3 MRI data acquisition and processing

Exams were acquired on the same 3T scanner (Magnetom Trio, Siemens Healthineers) and included a 3D T1-weighted sequence (≤1mm isotropic voxel-size) for volumetric analyses and a T2-weighted FLAIR sequence for the quantification of total demyelinating lesion volume (TLV). Sequence parameters and image processing steps are detailed in the Supplemental Material. Briefly, for all participants, demyelinating lesions were automatically segmented, visually checked, and where needed manually adjusted on FLAIR images to compute TLV, while T1-weighted volumes were used for an atlas-based parcellation of gray matter (GM) into 116 regions defined by the Automated Anatomical Labeling (AAL) atlas.[18]

2.2.4 Statistical Analysis

A flowchart summarizing data processing and analysis steps is depicted in Figure 2.1.

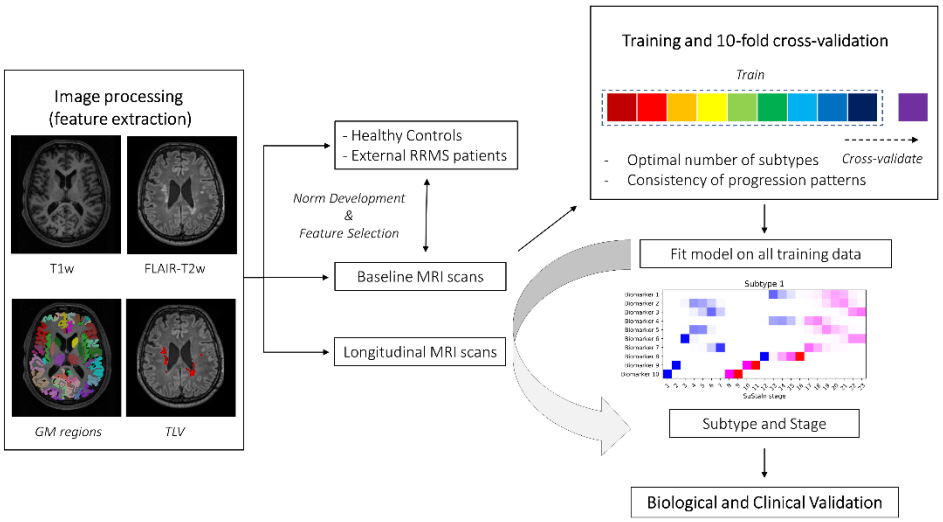

Figure 2.1. ***Workflow illustrating the main data processing and analysis steps.*** *Volumes of demyelinating lesions and 116 atlas-defined gray matter regions were automatically segmented based on FLAIR-T2w and T1-w images, respectively. Then, the corresponding volumes were expressed as z-scores with reference to external populations of patients and healthy controls, that were also used to select the most altered MRI-derived volumes. Following feature selection, baseline MRI biomarkers entered the Subtype and Stage Inference (SuStaIn) algorithm, using 10-fold cross-validation to determine the optimal number of subtypes and the consistency of progression patterns. Models of up to a maximum of 4 subtypes with z-scores of 1, 2 or 3 for each biomarker were tested (excluding z-score events reached by fewer than 5% of the subjects), corresponding to interpretable levels of mild, moderate and severe abnormality (color coded from blue to red). The trained model was then fit on all training data and applied to longitudinal MRIs. Finally, the biological reliability and clinical relevance of the SuStaIn classification were assessed in the light of longitudinal MRI scans and clinical outcomes.*

SuStaIn modelling

SuStaIn is an unsupervised machine learning algorithm combining ideas from clustering and event-based modelling, which describes disease progression as the linear evolution of biomarkers along discrete levels of cumulative alteration, defined in terms of deviation from a reference norm (z-scores).[8] It simultaneously estimates subgroups characterized by distinct patterns of biomarker evolution and the corresponding trajectories, providing a probabilistic assignment of each subject to a specific subtype and stage within a subtype. Methodological aspects of the SuStaIn algorithm are covered in *Young et al*.[8]

Briefly, MRI-derived GM and lesion volumes were expressed as z-scores with reference to the HS group and the external RRMS population, respectively, with signs of the z-scores flipped when appropriate so that higher values always represented disease worsening. Baseline MRI scans were used as the training set, while longitudinal visits were reserved for the biological and clinical validation of the initial classification.[8]

Only variables associated with a moderate to large (Cohen's $f>0.25$) difference between MS patients and HC were selected and entered the SuStaIn algorithm. Models were evaluated using 10-fold cross-validation (CV) in the training cohort to estimate the optimal number of subtypes and the consistency of the subtype progression patterns: the number of subtypes maximizing the average out-of-sample log-likelihood across CV folds was preferred; the similarity of each subtype progression pattern across CV folds (CVS) was measured using the Bhattacharyya coefficient.[8] Finally, the resulting model was fitted on all subjects of the training cohort and applied to unseen longitudinal MRI scans to assign a probable subtype and stage to each MRI visit.

Testing the biological reliability and clinical relevance of SuStaIn classification

The stability of the SuStaIn subtypes over time was expressed with

Krippendorf's α.[19] To assess the rate of change in disease stage, we fit a multilevel linear regression model in which the SuStaIn stage was the dependent variable and follow-up time (nested within subjects) the predictor, with intercepts and slopes allowed to vary across subjects (random effects). The possible effect of baseline subtype and stage on the slope of longitudinal stage change was assessed by separately adding them (and the corresponding interactions with follow-up time) to the model and testing the significance of interaction terms. Similar models were set up for individual MRI-derived biomarkers.

The clinical relevance of the SuStaIn classification was assessed in relation to both baseline EDSS and long-term clinical outcomes with ordinal/logistic regression (as appropriate) analyses, in which baseline subtype and stage and their interaction, age and sex were the independent variables. Follow-up time, baseline EDSS and disease-modifying therapy were included as additional covariates for longitudinal analyses.

Statistical analyses were carried out using the Statistical Package for Social Science (SPSSv25.0, IBM corp.).

2.3 Results

2.3.1 Participants

Four hundred and twenty-five RRMS patients (baseline age: 35.9±9.9 years; F/M: 301/124) were selected, corresponding to a total of 1129 MRI visits (2.7 MRI visits per patient, on average; range: 0 - 9), and a mean follow-up (FU) time of 2.1 years.

MRI scans of 148 HS (age: 35.9±13.0 years; F/M: 77/71) were also selected, along with those of an external population of 80 MS patients (age: 40.4±11.9 years; F/M: 56/24).

Demographic and clinical characteristics of the studied population are reported in Table 2.1.

	MS	HS	MS (external site)
Number of subjects	425	148	80
Number of MRI scans	1129	148	80
Age (y)	35.9±9.9	35.9±13.0	40.4±11.9
*Female Sex**	301 (70.8)	77 (52.0)	56 (70.0)
DD (y)	12.7±8.3	-	10.3±7.4
*EDSS***	2.5 (2.0 - 3.5)	-	2.0 (1.5 - 3.0)
TLV (ml)	10.1±13.4	-	3.4±5.3
WBV (ml)	1328.8±127.9	1385.1±147.4	1370.4±153.3

* Data are the number of subjects, with percentages in parentheses.
** Data are medians, with interquartile ranges in parentheses.

Table 2.1. ***Demographic, clinical and MRI characteristics of the studied population.***

Long-term clinical outcomes were available for 178 patients (level of motor disability: 0=121, 1=35, 2=16, 3=6; level of cognitive disability: 0=81, 1=42, 2=24, 3=31; transition to secondary progressive course: 29 subjects).

2.3.2 SuStaIn model

The volumes of 10 GM regions, including the bilateral anterior cingulate cortices, the right middle cingulate cortex, the bilateral insulae and cunei, the right putamen and the bilateral thalami, were associated with a moderate to large difference compared with the HC group and were thus fed into the SuStaIn algorithm along with TLV, for a total of 11 biomarkers (Figure 2.2).

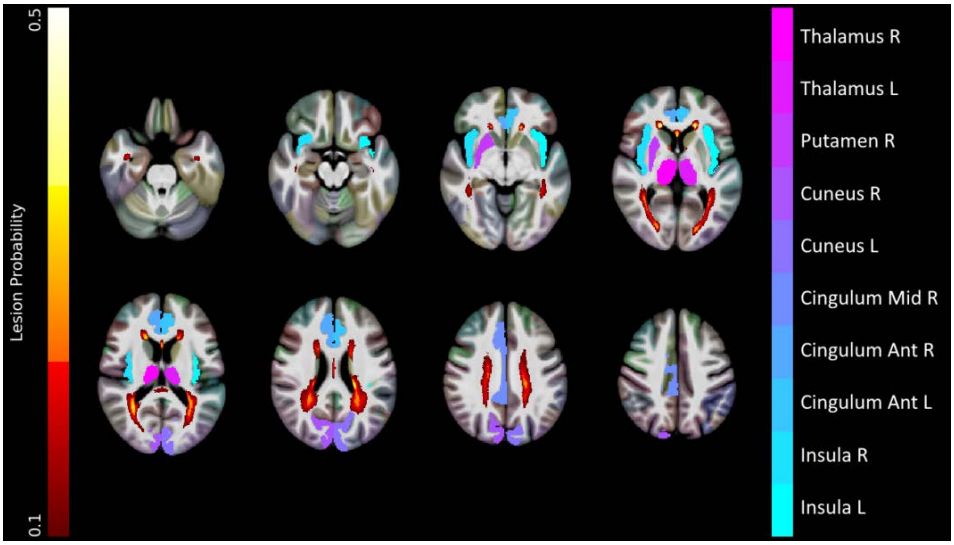

Figure 2.2. ***Results of the feature selection procedure.*** *Gray matter regions whose volume survived the feature selection procedure (i.e. associated with a moderate to large effect size at the comparison with healthy controls) are presented, along with a lesion probability map (obtained by summing all the binary lesion masks and dividing by the number of patients, thresholded at 10% probability), all superimposed on axial slices of the average T1w volume in the standard space. Images are in radiological orientation.*

The two-subtype model yielded the highest average log-likelihood across CV folds (Figure 2.3) and was therefore chosen as the best fitting model for subsequent analyses.

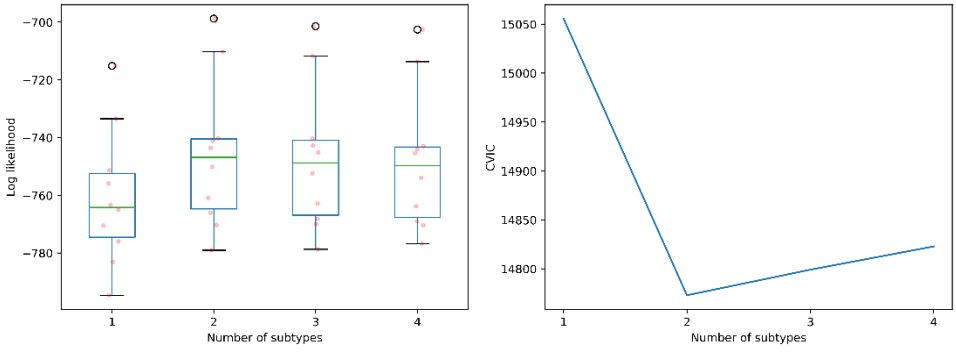

Figure 2.3. ***Results of the 10-fold cross-validation.*** *For models with different number of subtypes, values of log-likelihood (LL) on the test data for each cross-validation fold are presented (left panel), along with the corresponding average cross-validation information criterion (CVIC, defined as -2*LL) (right panel).*

When looking at the trajectories of brain damage progression in each

subtype, we designated them as follows: (1) the deep gray matter (DGM)-first subtype (56% of subjects, n=238), characterized by the initial volume loss of subcortical gray matter structures followed by lesion accrual and cortical atrophy and (2) the cortex-first subtype (44% of subjects, n=187), characterized by cortical volume loss preceding DGM atrophy and lesion accumulation (Figure 2.4).

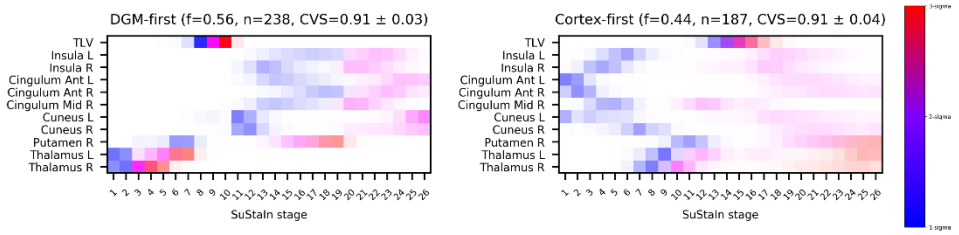

Figure 2.4. ***Positional variance diagrams for the two MRI-driven subtypes.*** *Each entry describes the probability for each biomarker of reaching the color-coded z-score at each SuStaIn stage. The colours represent the degree of abnormality based on the z-score level (blue=mild, z-score of 1; violet=moderate, z-score of 2; red=severe, z-score of 3), while the colour shade reflects the uncertainty associated with the corresponding biomarker event.*

Both progression patterns demonstrated high stability across CV folds, with CVS of 0.91±0.03 and 0.91±0.04 for the DGM-first and cortex-first subtypes, respectively (Figure 2.5).

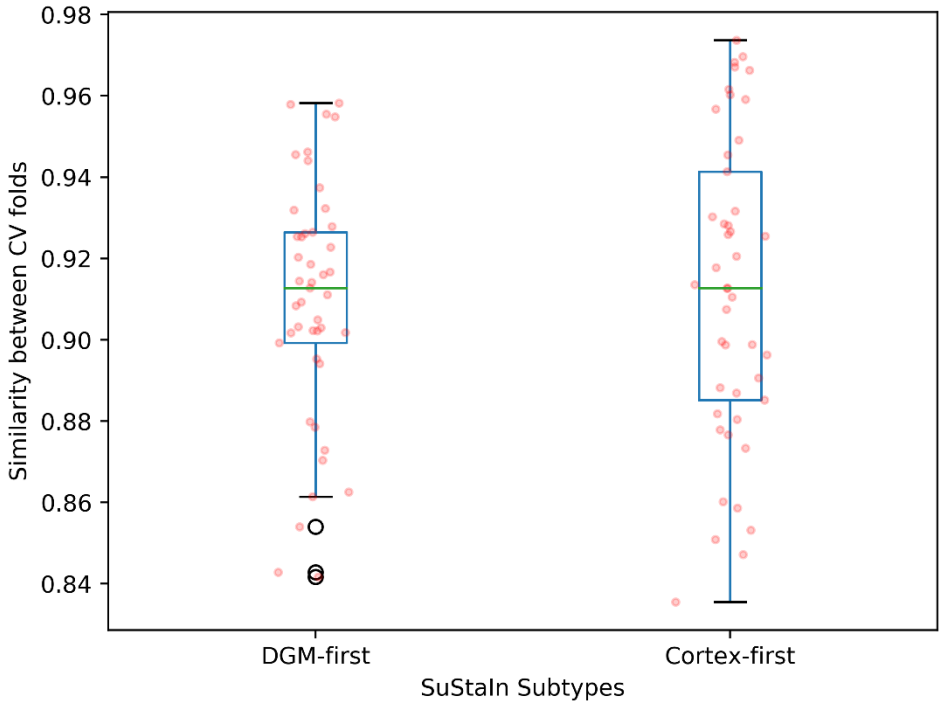

Figure 2.5. ***Reproducibility of subtypes under cross-validation.*** *The boxplots summarize the distribution of the similarity (Bhattacharyya coefficient) between subtypes estimated from each pair of cross-validation folds.*

Patients assigned to the two subtypes had comparable age, sex and whole brain volume (WBV), while the DGM-first subtype was associated with longer DD ($p<0.001$) and higher baseline EDSS score ($p=0.004$), SuStaIn stage ($p=0.01$) and TLV ($p<0.001$) (Table 2.2).

	DGM-first (56%, n=238)	Cortex-first (44%, n=187)	*p*-value***
Age (y)	35.9±10.1	35.9±9.5	0.98
*Female Sex**	160 (67.2)	141 (75.4)	0.36
DD (y)	9.4±7.8	6.5±6.1	**<0.001**
*EDSS***	2.5 (2.0-3.5)	2.5 (2.0-3.0)	**0.004**
SuStaIn stage	4 (1-12)	4 (1-8)	**0.01**
TLV (ml)	14.0±15.1	5.5±8.9	**<0.001**
WBV (ml)	1325.3±126.8	1333.0±129.5	0.65

Unless otherwise indicated, data are expressed as mean±standard deviation. Between-group differences were tested with either Student t (age and DD), Pearson Chi-square (sex), Kruskal-Wallis (EDSS and SuStaIn stage) or age-, sex- and TIV-corrected ANCOVA (TLV and WBV) tests.

** Data are the number of subjects, with percentages in parentheses.*

*** Data are medians, with interquartile ranges in parentheses.*

**** Significant between-group differences are reported in bold.*

Table 2.2. ***Demographic, clinical and MRI characteristics of the MRI-driven subtypes.***

2.3.3 Biological reliability and clinical relevance

Disease subtypes tended to be consistent over time (Krippendorf's α=0.806; CI=0.752,0.821), with subtype stability increasing as the probability threshold for the baseline subtype assignment was raised at 95% (177 subjects; α=0.990; CI=0.973, 0.998) or 99% (114 subjects; α=0.990; CI=0.973, 0.998).

In patients who retained the initial subtype, there was a significant annual increase in disease stage (b=0.20; SE=0.05; CI=0.09, 0.30; p<0.001), supporting the biological reliability of SuStaIn's staging, with no significant between-subtype difference (interaction term subtype*follow-up time: b=-0.08; SE=0.11; CI=-0.29, 0.13; p=0.48). A significant moderation effect of baseline stage on the relationship between follow-up time and disease stage was observed (interaction term baseline stage*follow-up time: b=-0.05; SE=0.01; CI=-0.08, -0.02; p=0.001), corresponding to slopes getting flatter as the baseline stage increased and probably reflecting a plateau effect.

When looking at individual MRI-derived biomarkers, all the GM volumes

significantly decreased over time (p≤0.03), with significant between-group differences for the left thalamus, corresponding to greater longitudinal atrophy rates in the DGM-first subtype (interaction term subtype*follow-up time: b=0.05; SE=0.01; CI=0.02, 0.07; p=0.001), and significant plateau effects (the higher the baseline stage the flatter the slope of longitudinal changes) for the right thalamus (interaction term subtype*follow-up time: b=0.007; SE=0.003; CI=0.002, 0.013; p=0.006) and the right anterior cingulate cortex (interaction term subtype*follow-up time: b=0.002; SE=0.001; CI=0.001, 0.003; p=0.002).

As for the relationship with clinical outcomes, baseline EDSS score was positively related with both SuStaIn stage (b=0.042; p<0.001) and the DGM-first subtype (b=-0.280; p=0.02), with baseline stage that also predicted long-term disability (b=0.030; p=0.007) and transition to SP course (b=0.079; p=0.03). Long-term cognitive impairment was associated with higher baseline stages (b=0.048; p<0.001), the DGM-first subtype (b=-0.442; p=0.005) and their interaction (b=-0.080; p=0.002).

2.4 Discussion

The ambition towards personalized medicine has stimulated increasing efforts to disentangle the inter-subject variability of neurological disorders, integrating information from different biomarkers to identify distinct underlying biological drivers (i.e. biotypes), up to the level of individual patients.[20] In this work, we obtained a biologically consistent and prognostically relevant stratification of RRMS patients based on the unsupervised modeling of brain volumetric features derived from cross-sectional MRI visits.

Using the SuStaIn algorithm, two distinct MRI-driven subtypes were identified, with a latent pattern in which early DGM atrophy and T2 lesion accumulation precede cortical atrophy separated from one in which cortical volume loss precedes DGM atrophy and lesion accrual. These

results are essentially in line with the recent work by *Eshaghi et al.*,[12] with slight dissimilarities most probably due to the different choices of input features. Indeed, the apparent discrepancy in terms of the number of subtypes is most likely explained by the lack of MRI-derived measures of normal appearing white matter damage in our study, which limited the sensitivity to capture the phenotypic heterogeneity associated with extra-lesional microstructural injury.

On the other hand, the application of a more fine-grained brain parcellation scheme led to a more anatomically precise modelling of GM atrophy, highlighting regions most prominently involved in MS such as the thalami and anterior cingulate, insular, and visual cortices.[10] Interestingly, the fact that distinct disease subtypes remain distinguishable based on the patients' MRIs even within a relatively clinically homogeneous population confirms the scarce correspondence between clinical and MRI-driven phenotyping, with the latter more closely reflecting disease-related pathogenic mechanisms.[12]

Indeed, while patients assigned to the two subtypes did not significantly differ in terms of age, sex, or WBV, the DGM-first subtype was associated with higher DD, stage and TLV, consistent with the idea of distinct pathogenic mechanisms underpinning cortical and DGM atrophy.[21–23] In particular, based on the closer association with TLV, subcortical GM might be more sensitive to the secondary effects of focal demyelination through anterograde/retrograde degeneration, with a prominent role of primary GM neuroinflammation and neurodegeneration in determining cortical atrophy.[22–24] Also, the longer DD suggest an earlier diagnosis in patients of the DGM-first subtype, possibly reflecting a shorter prodromal phase.[12,25]

The biological reliability of the MRI-driven classification was further confirmed by the analysis of longitudinal MRI scans, with high subtype stability and significant stage increase over time, reflecting actual

temporal progression of brain damage along the estimated paths. Also relevant in terms of biological consistency, moderation analyses suggested plateau effects in the longitudinal trajectories of SuStaIn stage and individual biomarkers (i.e. right thalamus and anterior cingulate cortex atrophy), in line with known temporal patterns of MS-related brain atrophy,[26,27] with steeper thalamic shrinkage rates in the DGM-first subtype.

When assessing the clinical relevance of the SuStaIn classification, higher baseline EDSS scores were independently associated with both higher stages, corresponding to more pronounced brain structural damage, and the DGM-fist subtype, a finding consistent with prior evidence pointing at the prominent role of subcortical GM (thalamic, in particular) atrophy in driving disability.[28,29]

As for the prognostic meaning of the MRI-driven stratification, patients in a more advanced position along the damage progression trajectory were more likely to enter the clinically progressive phase in the long term, as well as to suffer greater degrees of motor and cognitive disability, with more severe cognitive impairment also independently associated with the DGM-first subtype. These findings further corroborate the idea that, although cross-sectional in nature, the baseline MRI-driven classification encodes relevant information about future disease evolution, also substantiating the role of subcortical GM atrophy as a relevant anatomical correlate of cognitive disability in MS.[30,31]

Overall, the proposed approach provides insights into MS-related disease mechanisms, confirming and expanding the existing knowledge on MS physiopathology. But even more interestingly, it condenses this complex information at the patient level in simple and intuitive measures which are easily obtainable from single-visit conventional MRI scans and correlate with clinical measures of disease severity and progression. Contextualizing the information contained in individual brain MRIs in

the frame of disease patterns estimated in a reference population of MS patients, such stratification holds potential for effectively linking MS research to the single-subject setting, with relevant implications for both clinical trials and routine practice.

Our work is not without limitations. While the monocentric nature of the study reduces the data heterogeneity related to scanner/centre effects, it also limits the model generalizability, prompting larger studies on multicentric datasets. Furthermore, increasing the sample size would also allow for a higher dimensional (and more accurate) representation of MS pathology, possibly including additional biomarkers from spinal cord imaging or from other advanced MRI techniques encoding relevant information about the brain microstructure (e.g. diffusion MRI, quantitative MRI)[21,32] or function (e.g. functional MRI).[32]

In conclusion, through the unsupervised modelling of volumetric features derived from brain MRI scans, we obtained a biologically reliable and prognostically meaningful single-visit classification of MS patients, potentially offering a powerful tool for subjects' stratification in both trial design and clinical practice.

FRIDERICVS
IMPERATOR
AVGVST

Chapter 3

The Brain-Age Paradigm in Fabry Disease

3.1 Background and Rationale

FD (OMIM 301500) is a rare X-inherited lysosomal storage disorder characterized by the accumulation of catabolites in various cell types, resulting from the absent or markedly deficient activity of the enzyme α-galactosidase A (α-Gal A) and leading to damage and loss of function of especially the kidney, heart and brain.[33]

Involvement of the central nervous system is mainly characterized by vascular pathology, whose severity may greatly vary according to several factors, not all completely understood.[34] However, while the recommended follow-up of patients with FD includes brain MRIs, an accurate evaluation of FD-related brain damage is hampered by the lack of quantitative imaging biomarkers,[35] which also contributes to the uncertainty concerning the effect of recently introduced specific treatments on cerebral manifestations.[36]

In the search for objective imaging-derived markers of brain health and pathology, the brain-age paradigm has emerged as a promising approach. Briefly, machine learning methods are used to model chronological age as a function of structural brain MRI scans in healthy people, and the resulting model of 'normal' brain aging is used for neuroimaging-based age prediction in unseen subjects.[37] The extent to which each subject deviates from healthy brain-aging trajectories, expressed as the difference

between predicted and chronological age (brain-predicted age difference, brain-PAD), has been proposed as an index of structural brain health, sensitive to brain pathology in a wide spectrum of neurological and psychiatric disorders.[38]

As a relevant example, brain-age predictions are influenced by the presence of white matter hyperintensities (WMH) and brain volumes, imaging features that are both sensitive to cerebral small vessel disease,[39-41] which is thought to be one of the main neurobiological mechanisms through which FD impacts brain health.[34]

Here, we applied the brain-age paradigm to investigate neurological involvement in patients with FD. Our main aims were: i) to assess whether they have older-appearing brains compared to healthy controls (HC); ii) to validate brain-PAD as a measure of disease severity against other established clinical markers; iii) to explore the neuroimaging determinants of brain-age prediction in this condition.

3.2 Materials and Methods

3.2.1 Participants

In this retrospective, cross-sectional study, part of a larger monocentric research framework on the involvement of the central nervous system in FD, patients with a genetic diagnosis were selected,[42] along with age- and sex-comparable HS. To avoid the confounding effect of major cerebrovascular events, participants with a history of stroke or transient ischemic attacks were not included in this study. Additional exclusion criteria were age < 15 or > 65 years, and the presence of other relevant neurological, psychiatric or systemic conditions.

Scores quantifying the involvement of nervous, renal and cardiac systems in FD patients were computed based on clinical variables recorded within 1 month from the MRI and summed to obtain a cumulative measure of multi-organ damage severity, the total raw Fabry stabilization index

(FASTEX) score.[43]

The study was conducted in compliance with ethical standards and approved by the local ethics committee. Written informed consent was obtained from all subjects according to the Declaration of Helsinki.

3.2.2 MRI acquisition and preprocessing

All MRI examinations were performed on the same 3T scanner (Magnetom Trio, Siemens Healthineers), equipped with an 8-channel head coil. The acquisition protocol included a structural T1-weighted (T1w) volume acquired using a 3D magnetization prepared rapid acquisition gradient echo (MPRAGE) sequence (TR = 1900 ms; TE = 3.4 ms; TI = 900 ms; flip angle 9°; voxel size 1 x 1 x 1 mm^3; 160 axial slices) and, for FD patients, a T2-weighted 3D fluid attenuated inversion recovery (FLAIR) sequence for the assessment of WMH (TR = 6000 ms; TE = 396 ms; TI = 2200 ms; Flip Angle = 120°; voxel size = 1 x 1 x 1 mm^3; 160 sagittal slices).

For FD patients, WMH were automatically segmented on FLAIR images using Lesion Segmentation Tool (LST) 3.0.0 (www.statistical-modelling.de/lst.html).

We used the Computational Anatomy Toolbox (CAT12.8, http://www.neuro.uni-jena.de/cat) to segment T1w volumes into grey matter (GM), white matter (WM) and cerebrospinal fluid (CSF). Then, following the preprocessing steps of voxel-based morphometry (VBM), GM and WM probability maps were normalized to a 1mm isotropic template in MNI space, modulated with the Jacobian determinant derived from the spatial normalization and smoothed using a 1mm full width at half maximum isotropic Gaussian kernel.[44]

Summary volumetric measures of GM, WM, CSF, and total intracranial volume (TIV) were also generated, and brain parenchymal fraction (BPF) was computed as the ratio of brain volume to TIV.

3.2.3 Brain-age modelling

A model of healthy brain aging was trained and evaluated on a large dataset (total N: 2160; male/female: 1293/867; mean age: 33, age range: 4-86) comprising 3D T1-weighted brain scans of healthy subjects from 8 publicly available sources.

Raw T1w volumes underwent minimal preprocessing, including DICOM to NIfTI conversion, correction for intensity non-uniformity with N4BiasFieldCorrection,[45] rigid registration to the MNI152 space and resampling to 1.5 mm^3 voxels, to ensure consistency of spatial orientation and resolution. Furthermore, images were additionally cropped to reduce the array size to 118x142x118, and intensity-normalised by subtracting the image mean and dividing by the image standard deviation, using Project MONAI (https://docs.monai.io/en/stable/index.html).

Our brain-age model was based on the DenseNet264 architecture,[46] adapted from the implementation available at Project MONAI (https://docs.monai.io/en/stable/_modules/monai/networks/nets/densenet.html) by adding a linear regression layer for the prediction of a continuous variable and a 0.2 dropout rate after each dense layer to reduce the risk of overfitting. Briefly, DenseNet is a generalisation of the popular residual network (ResNet), which includes skip connections between internal neuron layers to overcome the vanishing gradient problem.[47] As achieving the best possible performance was beyond the objectives of our study, we decided to use an "off-the-shelf" standard DenseNet264 configuration, rather than designing a custom architecture, to ensure reproducibility and ease of use. Modeling was performed with PyTorch 1.12.0[48] using one NVIDIA Tesla V100S 32 GB graphics processing unit (GPU). The Adam optimizer was used to update model weights during training, with the learning rate initially set to 1e-4 and

decaying linearly as described in *Chen et al.*,[49] and additional L2 regularization at a rate of 1e-5. The full dataset was randomly split into training (64%=1382), validation (16%=346) and test (20%=432) sets. The batch size was 20 and the model was trained for 300 epochs: model checkpoints were saved after each epoch, and the model with the lowest validation loss was used for testing. Mean absolute error (MAE) and coefficient of determination (R^2) were used to quantify model performance. Lastly, age bias (i.e., underestimation of age in older subjects and vice versa) was statistically corrected as in *de Lange et al.*,[50] and the final model was applied to the internal cohort of FD patients and HC to generate brain-predicted ages and corresponding brain-PAD values.

An outline of the different steps of the brain-age modelling procedure is displayed in Figure 3.1.

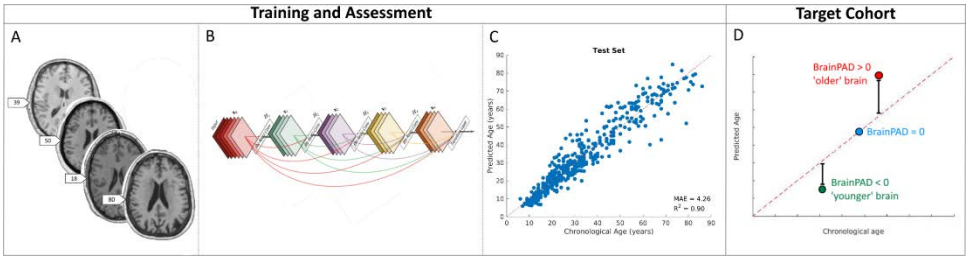

Figure 3.1. ***Outline of the brain-age modeling procedure.*** *Minimally preprocessed T1-weighted images (A) are used as input for the training and the evaluation of a model for the prediction of chronological age based on a 3D DenseNet architecture (B). The model with the lowest validation loss is chosen, and performance is measured on the previously unseen cases of the test set (C). The final model is also applied to the target clinical population (D), composed of the internal cohort of FD patients and HS, to generate brain-predicted ages and corresponding brain-PAD values.*

3.2.4 Statistical analysis

Unless otherwise specified, statistical analyses were carried out using the Statistical Package for Social Science (SPSSv25.0, IBM corp.), with a statistical significance level $\alpha = 0.05$ and 95% confidence intervals (CI) and

p values computed using bootstrap with 1000 resamples.

To assess possible between-group differences in terms of brain-PAD, we used one-way ANCOVA, controlling for the effects of age, age^2 and sex and calculating estimated marginal means for the two groups.

To validate brain-PAD as a measure of disease severity, we tested its association with the FASTEX score in a linear regression model including also age, age^2 and sex.

To investigate the neuroimaging determinants of brain-PAD in patients with FD, we used hierarchical linear regression analyses with age, age^2 and sex in the first block and WMH load or BPF in the second block. Similarly, age-, age^2- and sex-adjusted associations with brain-PAD were tested at the voxel level with TIV-scaled, preprocessed GM and WM maps, using a nonparametric approach based on 5000 permutations applied to the general linear model[51] via the Threshold Free Cluster Enhancement (TFCE) toolbox (http://www.neuro.uni-jena.de/tfce). The same analysis was repeated after adding the variables group (i.e., FD or HS) and group*brain-PAD interaction in the model, with this latter term intended to test the hypothesis that different voxel-wise patterns might influence brain-age prediction in the two groups.

3.3 Results

A total of 52 patients with FD were selected (40.6 ± 12.6 years; M/F: 24/28), along with 58 HC (38.4 ± 13.4 years; M/F: 30/28).

Demographic, clinical, and MRI characteristics of the studied population are available in Table 3.1.

	FD **N = 52**	**HS** **N = 58**	***p* value** **(FD vs HC)**
Age (y)	40.6 ± 12.6	38.4 ± 13.4	0.37
Sex (M/F)[1]	24/28	30/28	0.56
FASTEX score[2]			
Total score	6 (3 – 9)	n.a.	n.a.
Nervous system score	2 (1 – 2)		
Renal system score	1 (1 – 3)		
Cardiac system score	2 (1 – 3)		
BPF	0.81 ± 0.03	0.82 ± 0.03	0.06
WMH load (ml)	0.9 ± 3.7	n.a.	n.a.

Unless otherwise specified, data are expressed as mean ± standard deviation. Between-group differences were tested with either Student *t* (age and BPF) or chi-square (sex) tests.

[1] Expressed as number of subjects.

[2] Expressed as median, with interquartile range in parentheses.

Table 3.1. ***Demographic, clinical, and MRI characteristics of all the subjects included in the study.***

The brain-age model achieved accurate out-of-sample age prediction (test set MAE = 4.01, $R^2 = 0.90$).

When looking at brain-PAD values in the internal cohort, there was a significant effect of the group variable after controlling for age, age^2, and sex ($F[1, 105] = 6.46$, $p = 0.01$, partial $\eta^2 = 0.06$), with FD patients showing higher values than HC (estimated marginal means 3.1 [95% CI = 1.0 – 5.3] vs -0.1 [95% CI = -1.9 – 1.4]) (Figure 3.2).

A

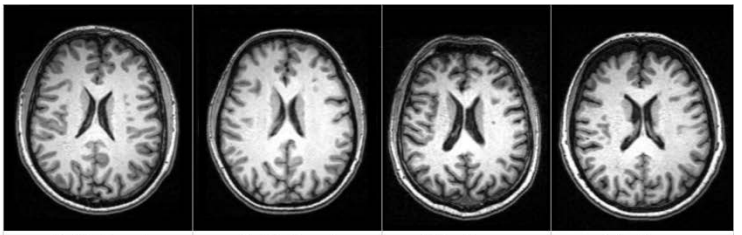

Group	Healthy Control	Healthy Control	Fabry Disease	Fabry Disease
Sex	Male	Female	Male	Female
Age (years)	42.0	46.5	39.1	46.0
Brain-Predicted age (years)	33.4	40.5	59.5	56.6
Brain-PAD (years)	-8.6	-5.9	20.4	10.6

B

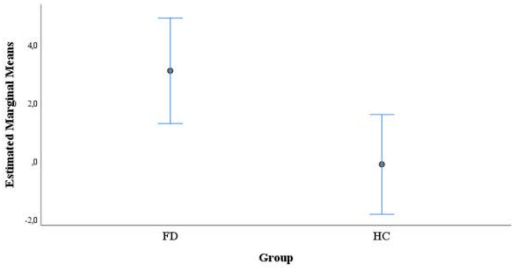

C

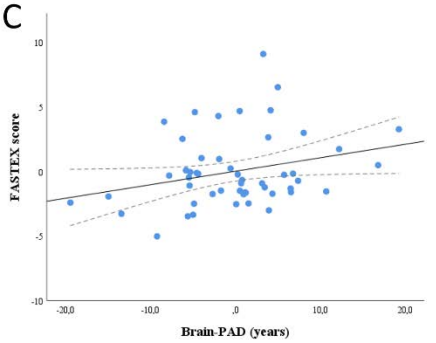

Figure 3.2. Brain-age prediction in the internal cohort and its relationship with disease status (FD vs HS) and the FASTEX score. *In (A), presented are comparable-level axial slices from four example subjects (two per group) with extreme brain-PAD values. In (B), age, age², and sex-adjusted estimated marginal means for the two groups, along with 95% bootstrap confidence intervals. In (C), scatterplot showing the relationship between brain-PAD values (age, age², and sex-adjusted) and FASTEX score in patients with FD.*

Brain-PAD was significantly associated with the FASTEX score (B = 0.10 [95% CI = 0.02 – 0.19]; standard error B = 0.04; p = 0.02), in a linear model including also age, age² and sex ($R^2 = 0.41$, $p < 0.001$) (Figure 3.2).

As for the neuroimaging determinants of brain-PAD in FD patients, both higher WMH load ($p = 0.01$) and lower BPF ($p = 0.001$) were associated with older-appearing brains (Table 3.2).

	B (95% CI)	SE B	*p*
Model 1			
Constant	10.48 (-6.00 – 35.60)	9.41	0.23
Age	-0.12 (-1.19 – 0.71)	0.54	0.82
Age^2	-0.002 (-0.016 – 0.017)	0.007	0.75
Sex	1.65 (-2.48 – 6.14)	2.13	0.45
Model 2			
Constant	8.53 (-7.32 – 39.21)	8.85	0.29
Age	0.04 (-0.94 – 0.73)	0.50	0.93
Age^2	-0.005 (-0.017 – 0.012)	0.006	0.43
Sex	0.53 (-3.37 – 4.13)	2.04	0.80
WMH load	0.85 (-2.35 – 6.78)	1.72	0.01
Model 3			
Constant	148.47 (77.24 – 224.90)	36.81	0.001
Age	-0.54 (-1.76 – 0.27)	0.54	0.30
Age^2	0.000 (-0.012 – 0.017)	0.007	0.96
Sex	0.71 (-3.21 – 4.86)	1.91	0.73
BPF	-153.50 (-236.42 – -73.24)	38.74	0.001

R^2 is 0.18 for Model 1, 0.32 ($\Delta R^2 = 0.14$) for Model 2, and 0.43 ($\Delta R^2 = 0.25$) for Model 3.

Table 3.2. Results of the hierarchical linear regression analyses for the prediction of brain-PAD in FD patients. *Confidence intervals, standard errors, and p values are based on 1000 bootstrap samples.*

Voxel-wise, we found a significant inverse correlation between brain-PAD values and tissue volumes diffusely throughout the brain, with the greatest effect sizes observed at the level of the deep and periventricular WM (Figure 3.3).

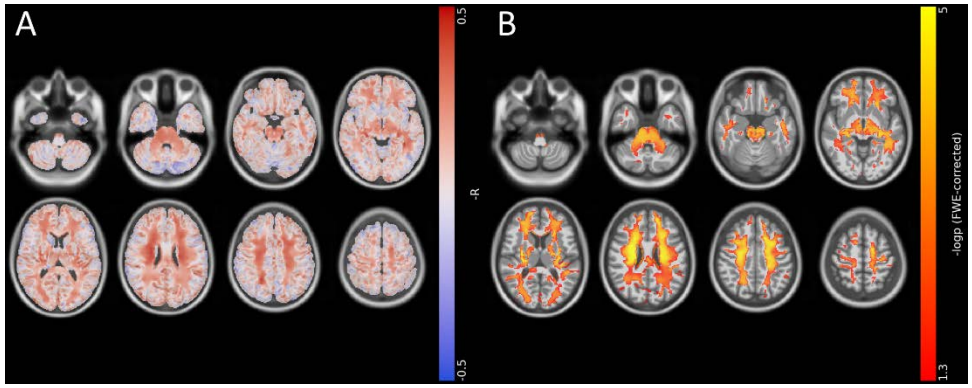

Figure 3. Voxel-wise correlation between brain tissue volumes and brain-PAD in patients with FD. *(A) Effect size (-R, red to blue) and (B) thresholded statistical (-logp, yellow to red) maps are shown, superimposed on axial sections of a 3D T1-weighted template in standard space.*

The interaction analysis revealed no significant effect of group on the relationship between local tissue volumes and brain-PAD.

3.4 Discussion

By applying the brain-age paradigm in a relatively large cohort of patients with FD, we found that indeed FD has an effect on the brain-PAD metric, indicative of accelerated brain aging, correlating with FD-related multi-organ damage and influenced by both (global) brain volumes and WMH load.

Notably, while we opted for an off-the-shelf standard network configuration, without focusing too much on hyperparameter tuning, the performance of the brain-age predictive model was not far from literature benchmarks.[52,53] Also, the model of healthy brain aging was sensitive to FD-related brain pathology.

Brain involvement in FD is thought to be mainly mediated by lysosomal deposition in endothelial cells, leading to microvascular (and sometimes macrovascular) manifestations that overlap those happening in common SVD and healthy aging.[34] More ambiguity exists on the possibility of direct brain tissue damage through lysosomal deposition at the level of

other cell types (i.e., neuronal or glial cells). Interestingly, the accumulation of lysosomal storage bodies in a subset of resident microglia is a physiological process that linearly increases with aging and seems to be accelerated in lysosomal storage disorders, leading to premature neurodegeneration.[54]

Taken together, these observations encourage the interpretation of FD as a form of accelerated brain aging, with brain-PAD as a possible marker of progressive brain damage.

On the other hand, it is known that FD is also a disorder of neurodevelopment,[55] and brain-age predictions can be heavily influenced by neurodevelopmental factors.[56]

Unfortunately, disentangling the contributions of neurodevelopmental factors from ongoing pathological processes is not completely possible in the cross-sectional setting. Assuming that the neurodevelopmental component remains constant over time, longitudinal studies are warranted where brain-PAD deltas ideally depend solely on ongoing healthy/pathological aging phenomena.

From the neuroimaging perspective, brain-PAD was influenced by WMH and (global) brain volumes, with no anatomical specificity other than the greatest effect sizes observed at the level of the deep and periventricular WM. Previous studies showed how brain-age prediction models are influenced by imaging features of small vessel disease, including WMH and GM volumes.[39–41] Also, our findings are in line with the evidence that global brain volume, rather than atrophy of specific regions, drives brain-age predictions.[52,53]

Interestingly, numerous structural MRI study with more conventional approaches (i.e., voxel-based morphometry, ROI analyses), failed to reveal consistent structural changes in FD patients compared to HS,[35,55,57] partly because of the small effect sizes and sample sizes. On the other hand, brain-PAD might be a more sensitive marker of brain structural

health, outperforming conventional methods.

Lastly, we found a significant association between brain-PAD and overall, multiorgan, clinical severity. Indeed, a not yet completely understood network of mutual interdependencies exists between brain age and other bodily "ages",[58,59] with the brain's structural health being strongly impacted by cardiovascular and renal (mal)functioning. This relationship also supports the potential role of brain-PAD as a quantitative biomarker for disease monitoring in clinical settings, with particular reference to the assessment of treatment response. In fact, the efficacy of the recently introduced specific treatments on cerebral involvement has remained unclear so far, partly precisely because of the lack of objective neuroimaging measures.

In conclusion, we demonstrate how brain-PAD is a sensitive measure of FD-related neurological and systemic involvement, bearing potential as a candidate biomarker of disease severity in clinical practice.

Chapter 4

Multimodal Brain Connectivity in Schizophrenia

4.1 Background and Rationale

SZ is a chronic, multifactorial psychiatric disorder that affects around 1% of the population, frequently leading to long-term functional impairment that impedes social and occupational integration.[60]

Alongside positive and negative symptoms, cognitive dysfunction is a core feature of SZ, with verbal memory being one of the most prominently affected domains2.[61] Indeed, verbal memory deficits often precede the onset of full-blown psychosis, tend to remain stable throughout the disease course, and are consistently among the best predictors of functional outcomes, thus representing an important treatment target.[62]

From the neuroimaging perspective, in the search for biomarkers of SZ that could inform clinical decisions, attempts have been made to link verbal memory impairment to regional brain structural modifications, such as hippocampal volume loss[63] or cortical thinning of the parahippocampal gyrus and the frontal cortex,[64] or to altered task-related functional activation.[65]

On the other hand, mapping symptoms to specific brain regions might be simplistic as we know by now that clinical functioning corresponds more closely to networks of connected regions, with regional deviations in

different locations potentially underlying the same clinical diagnosis due to dysfunction of common neural circuits.[66]

Since the formulation of the disconnection hypothesis in the 1990s,[67] numerous studies have consolidated our understanding of SZ as a network disorder, demonstrating modifications of structural and functional brain networks, mostly independently of each other, and putting them in relation to cognition.[68,69]

Nevertheless, results have often been conflicting, somehow failing to identify consistent imaging-based signatures of SZ and SZ-related cognitive dysfunction.[70] While this is partly explained by the intrinsically heterogeneous genetic, neurobiological, and phenotypic profile of SZ,[71] methodological issues might also play a role, including the disparateness of image processing strategies and the focus on single modality networks, providing only a partial grasp of the brain complex organization.

In this light, integrating different neuroimaging modalities holds the potential to enrich our understanding of the brain and its disorders, by informing us about how brain structure shapes brain function, how they are jointly impacted by disease, and which aspects are relevant for clinical functioning.[72]

Here, using two complementary data-driven approaches (i.e., threshold-free network-based statistics, TFNBS, and hybrid connectivity independent component analysis, connICA) for the analysis of diffusion (dMRI) and resting-state functional (RS-fMRI) MRI data, we explored joint modifications of structural and functional brain networks in patients with SZ, aiming to unveil the multimodal connectomics substrates of SZ-related verbal memory impairment.

4.2 Materials and Methods

4.2.1 Participants

In this prospective cross-sectional study, we recruited patients with SZ

diagnosed according to the DSM-5, along with age- and sex-comparable HS.

Inclusion criteria for patients were: age between 18 and 60 years; disease duration > 2 years; no medication switch or dose changes in the last 6 months (i.e., >10% baseline dose); no evidence of current or recent (3 months) worsening of psychotic symptoms; absence of macroscopic brain structural anomalies or other major systemic, psychiatric or neurological disorders.

Exclusion criteria for HS were: history of neurological, psychiatric or systemic conditions, current or lifetime substance or alcohol dependency, lifetime intake of psychotropic medication.

The study was conducted in compliance with ethical standards and approved by the local ethics committee (protocol number: 195/19). Written informed consent was obtained from all subjects according to the Declaration of Helsinki, revised Hong Kong 1989.

Clinical data were collected within one month from the MRI. Antipsychotic doses were transformed into chlorpromazine (CPZ) equivalents,[73] while the severity of psychotic symptoms was measured using the Positive and Negative Syndrome Scale (PANSS).[74] Additionally, verbal memory was assessed via the List Learning task, with raw data adjusted according to normative values of the Italian population.[75] Corrected scores were fitted into a 5-point scale to collect equivalent scores, based on which patients were classified as having impaired (VMI, score from 0 to 1), or preserved (VMP, score ≥ 2) verbal memory.[75]

All subjects performed a 3T MRI brain scan on the same 3T scanner (Magnetom Trio, Siemens Healthineers, Erlangen, Germany), equipped with an 8-channel head coil. The acquisition protocol included: a T1-weighted volume acquired using a 3D magnetization prepared rapid acquisition gradient echo (MPRAGE) sequence (TR = 1900 ms; TE = 3.4 ms; TI = 900 ms; flip angle 9°; voxel size 1 x 1 x 1 mm^3; 160 axial slices),

used as anatomical reference; diffusion weighted images acquired using a spin echo EPI sequence (TR = 7400 ms; TE = 88 ms; flip angle = 90°; voxel size = 2.2 × 2.2 × 2.2 mm^3 with 64 directions at b = 1000 s/mm^2 in addition to 9 b = 0 s/mm^2), for the analysis of structural connectivity (SC); T2*-weighted volumes acquired using a gradient echo EPI sequence (TR = 2500 ms; TE = 50 ms; voxel size = 3 x 3 x 4 mm^3; gap = 1 mm; 200 time points; 30 axial slices), for the analysis of functional connectivity (FC).

4.2.2 MRI data processing

Details of image processing pipelines are explained in the Supplementary Material.

Structural MRI and brain parcellation

Intensity nonuniformity-corrected, skull-stripped T1w volumes were used as anatomical reference throughout the diffusion and functional workflows. Additionally, through a registration-based procedure, the brain was parcellated into 100 cortical[76] and 16 subcortical[77] atlas-defined regions, used as a common set of nodes for the construction of connectivity matrices. Brain parcels are also associated with seven canonical cortical resting-state networks (RSNs) including the visual (VIS), somatomotor (SM), dorsal attention (DAN), ventral attention (VAN), limbic (L), control (CONT), and default mode (DMN) networks,[78] plus a network of subcortical regions (SUBC).

Diffusion MRI and anatomical brain networks

Preprocessing of dMRI data (including denoising, B1 field inhomogeneity correction, head motion, eddy current and susceptibility distortion correction and registration to the T1w volume) was performed using QSIPrep 0.14.3.[79] From preprocessed DWI data, constrained spherical deconvolution-based probabilistic tractography was carried out using anatomical constraints to generate a 10 million streamlines whole-brain tractogram. Finally, weights for each streamline were calculated through

a filtering procedure and a 116 x 116 SC matrix was filled with the sums of weights of streamlines connecting each node's pair.

In addition, structural matrices were $\log_{10}$-transformed to better account for differences at different magnitudes and to make the distribution of edges' weight more comparable to functional matrices.

Resting-state functional MRI and functional brain networks

Preprocessing of RS-fMRI data was performed using fMRIPrep 20.2.6[80] and included head motion, susceptibility distortion and slice-timing correction, registration to the T1w volume and denoising to minimize the residual non-neuronal variability of functional data.

Finally, mean "clean" BOLD time series were extracted from the atlas-defined parcels, and, for each node's pair, the Pearson correlation coefficient was computed and Fisher z-transformed to fill a 116 x 116 FC matrix. In addition, matrices were absolutized as inverse correlations may encode relevant information and most analysis strategies tend to neglect negative values.

Statistical analyses

Before entering second-level analyses, connectivity matrices were normalized using a singular-value decomposition approach to account for differences in average connectivity weight.[81]

Unless otherwise specified, statistical analyses were performed using R (version 4.1.2) and RStudio (version 2021.09.1).

TFNBS

To assess the presence of statistically significant effects in connectivity matrices, we used a TFNBS approach,[82] as implemented in MRtrix3's connectomestats. Briefly, TFNBS combines NBS[83] with threshold-free cluster enhancement,[84] augmenting edge-wise statistics based on the strength of effects occurring in topologically neighboring network edges and obviating the need for the a priori definition of a component-defining

statistical threshold. A p-value can be ascribed to each TFNBS-enhanced edge and corrected for multiple comparisons across the connectome.

F-tests were used for comparisons between subjects with SZ and HS and between VMI and VMP patients, with age and sex as nuisance variables. Five-thousands permutations were used, with a statistical significance level set at $p<0.05$ (FWER-corrected).

Hybrid connICA

To explore possible modifications of joint structural-functional connectivity patterns, we used a hybrid connICA approach[85] (https://engineering.purdue.edu/ConnplexityLab). Briefly, structural and functional networks are merged into a common hybrid matrix, which is fed into an ICA decomposition procedure to extract fundamental joint connectivity traits, estimated at group level, and subject-level projections, expressing the relative weight of each hybrid pattern in the individual connectivity profile.[85]

Here, we applied PCA to compress and reduce the dimensionality of the data by keeping the principal components explaining 90% of the variance of the initial hybrid data. Next, ICA decomposition was applied by running the FastICA algorithm to obtain 10 independent components. To account for the non-deterministic nature of the FastICA procedure, we evaluated the robustness of the traits over 100 FastICA runs. A hybrid trait was considered robust when it appeared (correlation of 0.75 or higher across runs) in at least 75% of the runs and its representation consisted of the average across all its appearances over the 100 runs.

Finally, individual weights for the identified robust components (RC) were adjusted for the effect of age and sex estimated in HS and compared between groups (SZ vs HS and, for SZ-related components, VMI vs VMP) using bootstrapped t-test with 1000 resamples, with a statistical significance level set at $p<0.05$ (FWER-corrected).

4.3 Results

4.3.1 Participants

A total of 49 patients with SZ were recruited (37.5 ± 9.7 years; M/F: 34/15), along with 55 HC (42.4 ± 15.7 years; M/F: 30/25).

Demographic and clinical characteristics of the studied population are available in Table 4.1.

	SZ N = 49	**HS N = 55**	**p value (SZ vs HS)**
Age (y)	37.5 ± 9.7	42.4 ± 15.7	0.06
Sex (M/F)*	34/15	30/25	0.18
Age of onset (y)	21.9 ± 6.8	n.a.	n.a.
Duration of illness (y)	14.7 ± 8.2	n.a.	n.a.
CPZ equivalents	453.3 ± 270.9	n.a.	n.a.
PANSS score			
Total	85.5 ± 17.2	n.a.	n.a.
Positive	19.2 ± 5.3	n.a.	n.a.
Negative	22.3 ± 5.9	n.a.	n.a.
General	44.0 ± 9.8	n.a.	n.a.

Unless otherwise indicated, data are expressed as mean±standard deviation. Between-group differences were tested with either Student *t* (age) or chi-square (sex) tests.

* Expressed as number of subjects.

Table 4.1. ***Demographic and clinical characteristics of all the subjects included in the study.***

Neuropsychological evaluation was performed for 48 patients, that were classified as either VMI (N = 26) or VMP (N = 22). The two subgroups did not significantly differ in terms of basic demographic and clinical variables (Table 4.2).

	VMI N = 26	**VMP N = 22**	**p value (VMI vs VMP)**
Age (y)	35.7 ± 9.0	39.1 ± 10.3	0.24
Sex (M/F)*	19/7	15/7	0.96
Age of onset (y)	19.9 ± 6.3	22.6 ± 7.2	0.18
Duration of illness (y)	14.4 ± 9.4	15.0 ± 7.0	0.81
CPZ equivalents	503.0 ± 269.2	403.1 ± 272.3	0.21
PANSS score			
Total	88.6 ± 18.9	82.14 ± 14.8	0.20
Positive	20.3 ± 5.9	18.1 ± 4.3	0.15
Negative	22.9 ± 6.7	21.7 ± 5.0	0.48
General	45.4 ± 10.7	42.4 ± 8.5	0.29

Unless otherwise indicated, data are expressed as mean±standard deviation. Between-group differences were tested with either Student *t* (age, age of onset, duration of illness, CPZ equivalents, PANSS scores) or chi-square (sex) tests.

* Expressed as number of subjects.

Table 2.2. ***Demographic and clinical characteristics of patients with impaired (VMI) or preserved (VMP) verbal memory.***

4.3.2 TFNBS

When looking at possible SC differences, distributed alterations emerged in patients with SZ, with both decreased and increased integrity of anatomical connections compared to HC (Figure 4.1).

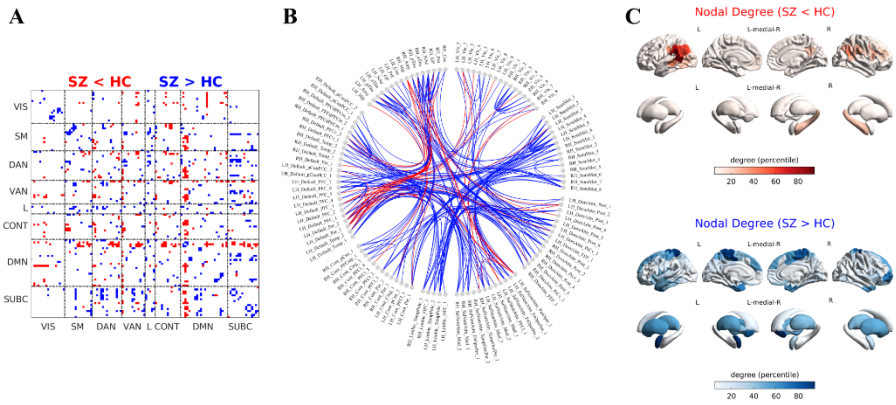

Figure 4.1. ***Network-based analysis of structural connectome between patients with SZ and HC.*** *The thresholded statistical matrix is shown (A), along with a circular graph representation of supra-threshold edges (B) and a surface render of the corresponding nodal degrees (C). Throughout the panels, color encodes the direction of observed changes (in red: SZ < HC; in blue: SZ > HC).*

As for the analysis of FC, a relatively circumscribed pattern of reduced within- and between-network connectivity encompassing the VIS and SM networks was observed, along with stronger functional connections between the VIS and non-sensorimotor networks and within- and between- cortical association and subcortical networks (Figure 4.2).

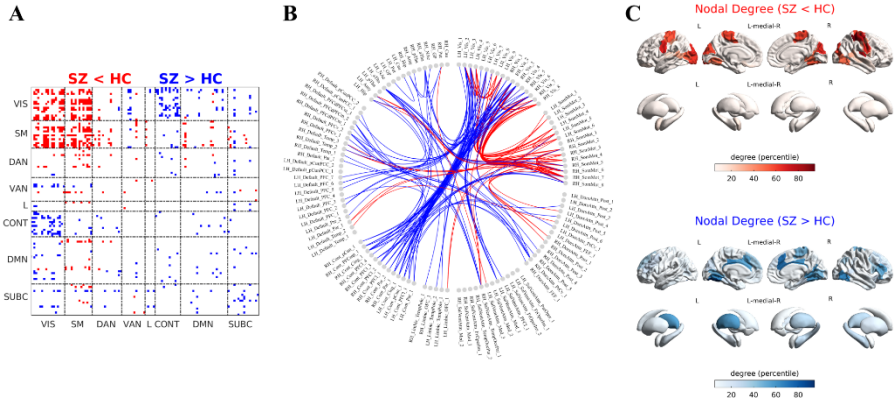

Figure 4.2. ***Network-based analysis of functional connectome between patients with SZ and HC.*** *The thresholded statistical matrix is shown (A), along with a circular graph representation of supra-threshold edges (B) and a surface render of the corresponding nodal degrees (C). Throughout the panels, color encodes the direction of observed changes (in red: SZ < HC; in blue: SZ >*

HC).

Regarding the relationship between brain connectivity and verbal memory, no significant effects were detectable for SC, with only two edges of significant FC increase in VMI compared to VMP patients connecting the VIS network with the posterior hubs of the DAN bilaterally.

4.3.3 Hybrid connICA

When looking at hybrid structural-functional connectivity traits, we identified 4 RCs. One of these, RC4, mainly driven by the FC part and capturing the connectivity of the VIS network, was significantly less represented in patients with SZ, with reduced average weight compared to HCs (Cohen's d = 0.828, $p < 0.0001$) (Figure 4.3).

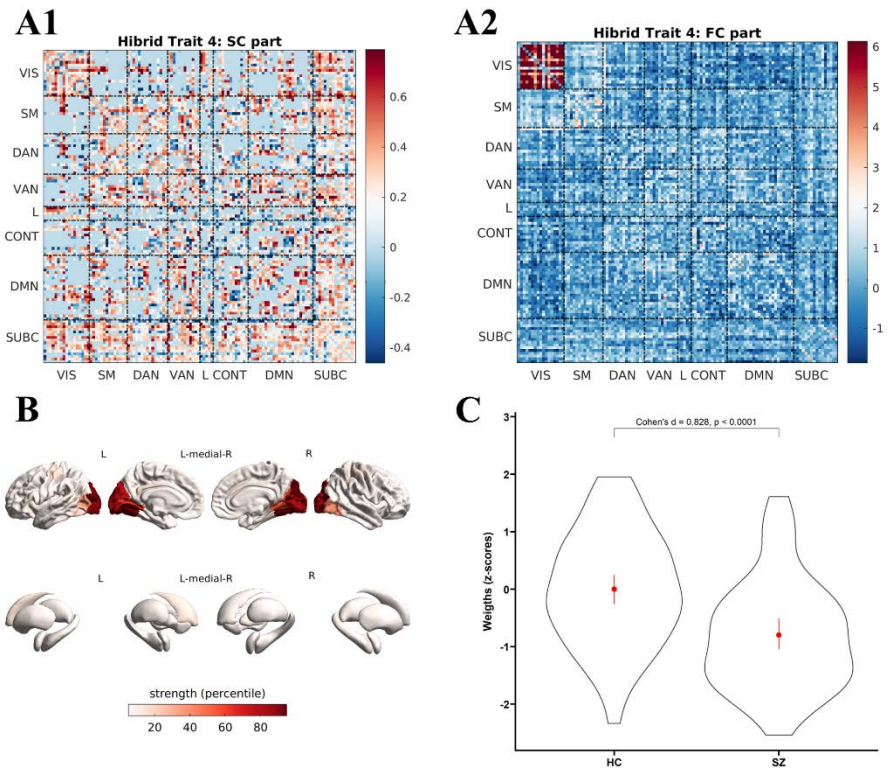

Figure 4.3. ***SZ-related hybrid structural-functional trait.*** *The hybrid trait 4 is shown, split in structural (A1) and functional (A2) connectivity matrices. To obtain an anatomical representation of the trait, nodal strength was computed on*

the absolutized, thresholded (top 10% edges) hybrid matrix, and visualized onto a surface render of the brain (B). (C) Violin plot showing the distribution of the hybrid trait's individual weights for SZ and HC subjects.

For RC1, mainly mapping the connectivity of frontotemporal poles and deep GM regions, a weaker difference between SZ and HC subjects was observed (Cohen's d = -0.403, p = 0.02, not significant after multiple testing correction). The remaining traits, mostly capturing the connectivity of the CONT network and the DMN, did not exhibit between-group differences.

RC4 was also sensitive to verbal memory deficits, with VMI patients showing higher average weight compared to VMP ones (Cohen's d = -0.805, p = 0.01) (Figure 4.4).

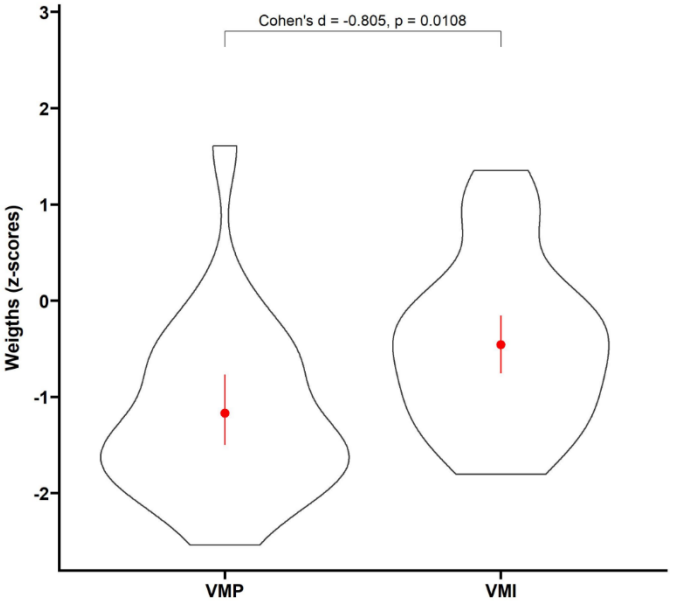

Figure 4.4. ***Association between hybrid trait 4 and verbal memory.*** *Violin plot showing the distribution of the individual weights for the SZ-related structural-functional trait in VMI and VMP SZ patients.*

4.4 Discussion

Using two complementary data-driven approaches, we investigated structural and functional brain networks in patients with SZ, both

separately and in conjunction, demonstrating widespread connectivity alterations and identifying deviations of the connectomic profile that might be specifically associated with verbal memory deficits.

We found distributed modifications of anatomical connectivity compared to HCs, with mixed patterns of hypo- and hyperconnectivity, both within and between large-scale functional networks.

Although the neurobiological basis of SC changes in SZ is not completely understood, also due to the possible effects of confounding factors like antipsychotic treatment, it is known that WM alterations are present from the prodromal to the chronic stages, with abnormal neurodevelopment representing the most plausible underlying mechanism.[86] Interestingly, several lines of evidence pointed to alterations of oligodendrocytes number and function in patients with SZ, possibly influencing synaptic formation and ultimately leading to functional and clinical impairment.[87,88]

In our sample, against the background of a widely deviating anatomical connectivity profile, a pattern of disrupted SC was observed encompassing prefrontal, parietal, and temporal regions subserving the DMN, as well as the hippocampi, which are also known to participate in the DMN.[89] Indeed, the DMN is known to play a pivotal role in SZ,[90] and anatomical connection deficits have been already demonstrated both between DMN nodes and between them and functionally anti-correlated networks,[91,92] likely resulting from aberrant maturation[93] and leading to functional reorganization.[90]

On the other hand, some stronger structural connections in SZ patients compared to HCs were also observable, mainly mapping onto deep GM structures (primarily thalami and amygdalae), superior frontal gyri, paracentral lobules, and temporal poles.

Indeed, evidence of increased anatomical connectivity in SZ has been reported multiple times,[68] with more recent studies highlighting the

involvement of subcortical pathways, such as the thalamocortical connections[94–96] and the medial forebrain bundle.[97]

In line with some of these works, we found increased SC between the thalami and sensorimotor regions, coupling with a stronger FC between the same areas, which has been also previously reported.[94,98] These observations are consistent with the hypothesis of thalamic dysfunction being a central neurobiological feature of the disease and contributing to psychotic symptomatology,[99] given the crucial role of the thalami not only as a relay station of sensorimotor information, but also as a critical hub for multimodal processes integration.[100]

From a functional standpoint, as expected, we found relatively widespread reorganization of large-scale brain networks in patients with SZ.

We identified a pattern of decreased within- and between-network FC specifically involving the VIS and SM networks. Functional changes in cortical areas implicated in primary sensory and motor processing have been largely described in SZ,[101] supposedly underlying not only psychomotor and basic perceptual alterations, but also impairment of higher-order functions through a bottom-up process.[102,103] In keeping with this hypothesis, increased FC was also observed between the VIS and cortical association networks and subcortical regions, respectively.

Stronger functional connections between visual regions and the DMN, responsible for introspection and self-referential processes,[104] and "task-positive" cortical regions (i.e., the CON and attention networks), generally involved in top-down control of goal-directed activities,[104] are known features of SZ,[105] possibly resulting from a failure of large-scale networks segregation during neurodevelopment.[106]

These alterations, along with the observed FC increase between the VIS and the thalami, which has been previously implicated in attention impairment in SZ,[98] may represent the neurobiological substrate of

aberrant sensory processing and integration, whose proper functioning relies on both voluntary shifts in directed attention, with efficient switching between unconscious and conscious visual perception,[107] and coherent top-down prior expectations.[108]

In this context, dysconnectivity of the CON and DAN, involved in visuospatial attention and exerting top-down modulation of context-relevant information encoding,[109] appears to play a central role, possibly feeding a positive feedback loop of abnormal perceptions and aberrant higher order cognitive processes.[108]

Confirming the possible maladaptive role of the observed functional reorganization, a tiny cluster of increased FC between the VIS network and posterior hubs of the DAN bilaterally was associated with impairment of verbal memory in SZ patients.

When investigating patterns of joint structural-functional connectivity, we identified a hybrid trait (RC4) that was significantly associated with SZ, mainly capturing VIS network-related FC.

Reduced representation of this component in patients with SZ compared to HCs substantially matches the results of single-modality analyses, further suggesting that a deviating connectivity profile of sensorimotor networks might be a core connectomic feature of SZ.

RC4 was also sensitive to verbal memory deficits, with a higher representation in VMI compared to VMP patients and a more conspicuous effect relative to single-modality network-based comparisons.

Whereas the direction of observed changes could appear counterintuitive (RC4 is less represented in subjects with SZ compared to HCs, but more represented in VMI compared to VMP patients), a context-dependent non-monotonic behavior might be hypothesized for this feature, with the hybrid trait's individual representation likely to have different (mal)adaptive roles according to the stage of the disease and the overall

connectomic profile.

Again, this finding supports the theory that aberrant connectivity of areas involved in primary sensory processing might induce deficits that reverberate to higher cognitive functions through a bottom-up process.[102,110,111]

Also, while it is clear that hybrid traits are dominated by variance in functional rather than structural edges, our results show that multivariate, multimodal approaches (compared to univariate, single-modality) may yield increased sensitivity towards disease-related deviations from the healthy connectome and a closer correspondence between brain networks and clinical functioning, given their ability to capture higher-order connectivity patterns[15].

The present study is not without limitations. First, since the patients' population was composed exclusively of chronic SZ subjects, we were not able to disentangle the possible effects of antipsychotic drugs on the observed brain networks' changes (although the two SZ subgroups did not significantly differ in terms of CPZ equivalents), nor to infer the possible role of disease stage. Thus, future studies are warranted to confirm the findings in first-episode, treatment-naïve SZ patients and high-risk subjects. Furthermore, given the cross-sectional nature of the study, the causal relationship between brain networks' changes and functional impairments could not be fully investigated, with longitudinal designs that would allow to assess the prognostic ability of connectomic modifications to predict clinical outcomes.

In conclusion, while we are still far from a comprehensive understanding of the neural substrates of SZ and SZ-related cognitive dysfunction, using multimodal MRI we identified a symptom-specific connectomic signature of the disease. We suggest that aberrant connectivity of sensorimotor networks may be a core feature of SZ and a putative biomarker of verbal memory impairment, with potentially relevant clinical implications in

terms of disease monitoring and treatment targeting.

Chapter 5

Quantitative MRI in Multiple Sclerosis

5.1 Background and Rationale

In MS, the physiopathological mechanisms behind atrophy accrual and its impact on disability have been investigated and confirmed by several independent groups.[22] Nevertheless, the nature and clinical relevance of tissue microstructural abnormalities remain more elusive, partly because the coexistence of different pathological processes (demyelination, inflammation, axonal loss) represents a challenge for their characterization.[112] In recent years, semi-quantitative and quantitative MRI methods have been developed to explore the nature of microstructural abnormalities, with particular interest in MS being devoted to the assessment of iron and myelin, as these might offer a glimpse into the neurodegenerative process and tissue repair capability.[113,114] Indeed, although iron accrual has to be interpreted with caution given the confounding effect of concomitant tissue loss,[115,116] iron depletion in WM and in WM-rich structures such as the thalamus likely results from oligodendrocytes dysfunction and damage, with reduced myelination capacity and trophic support leading to neurodegeneration.[117] Among quantitative parameters, histological validation studies have confirmed the applicability of quantitative susceptibility mapping (QSM) for the assessment of iron content in the basal ganglia, where myelin intensities have almost no effect on

susceptibility.[118] Within myelin rich structures such as WM and thalamus however, interpretation of susceptibility modifications are more challenging, as diamagnetic myelin and paramagnetic iron play opposite effects on susceptibility. In these regions a susceptibility increase would be expression of iron accrual/demyelination, while a susceptibility decrease would be expression of iron depletion/increase in myelin content.

Another quantitative parameter, which more closely reflects tissue myelin content, is the longitudinal relaxation rate (R1). R1 is strongly associated with both myelin and axon content,[119] but, according to postmortem analysis of brain tissue, it is primarily dependent on myelin content[120] and is among the most reliable myelin-sensitive MRI metrics.[114] Beyond the information that susceptibility and R1 changes (as proxies of iron and myelin content) can provide on the nature of microstructural abnormalities in MS, the clinical impact of such modifications remains unclear for several reasons. First, previous studies applying iron and myelin imaging in MS have mainly focused on global disability outcomes,[121,122] or have limited their investigation to selected regions of interest.[123,124] Second, the fact that correlations with disability might be driven by atrophy rather than modifications in iron and myelin per se has been rarely investigated.[116] Therefore, the goal of our work was to build on previous findings by exploring the impact of R1 and susceptibility changes on a wide range of disability outcomes (considering also manual dexterity and cognitive function), while accounting for atrophy, which is the main driver of disability accrual in MS and, as recently highlighted, has a major impact on qMR measures.[116,125] To this aim we conducted a multi-parametric analysis of quantitative MR, together with brain volumetry, to (i) characterize the topographical distribution of atrophy, R1 and χ changes in the MS brain and (ii) clarify their impact on both cognitive and motor disability.

5.2 Materials and Methods

5.2.1 Subjects

In this cross-sectional study, from February 2016 to January 2020, we prospectively enrolled MS patients diagnosed according to the 2010-McDonald criteria,[13] along with age- and sex-comparable HS.

The study was conducted in compliance with ethical standards, approved by the local Ethics Committee and written informed consent was obtained from all subjects according to the Declaration of Helsinki.

5.2.2 Clinical and Neuropsychological Assessment

Within one week from the MRI, patients' clinical disability was quantified using the Expanded Disability Status Scale (EDSS) score,[126] with disease course classified according to *Lublin et al*.[14] At the same time, patients were tested using the Symbol Digit Modalities Test (SDMT)[16] to assess cognitive processing speed, while ambulation and manual dexterity were probed through the Timed 25-Foot Walk (T25FW) and the 9-Hole Peg Test (9-HPT), respectively. SDMT scores were expressed as Z-scores with reference to normative values in the healthy population, adjusting for age, gender and education.[16] Similarly, T25FW and 9-HPT scores were referenced to normative values of an external population of MS patients[127] and averaged to obtain a single composite measure of motor performance. Z-scores were flipped, as appropriate, to have higher scores always corresponding to better performances.

5.2.3 MRI data acquisition and preprocessing

All MRI exams were performed on the same 3T scanner (Magnetom Trio, Siemens Healthineers) and included a 3D T1-weighted sequence for volumetric analyses, a 3D T2-weighted FLAIR sequence for T2-hyperintense lesions detection and lesion load (T2-LL) quantification and two spoiled gradient echo sequences for quantitative analyses.[128] Details about acquisition parameters and a thorough description of image

preprocessing, including the computation of R1 and QSM maps, are provided in previous publications,[128–132] while a flowchart summarizing the main image processing and analysis steps is depicted in Figure 5.1.

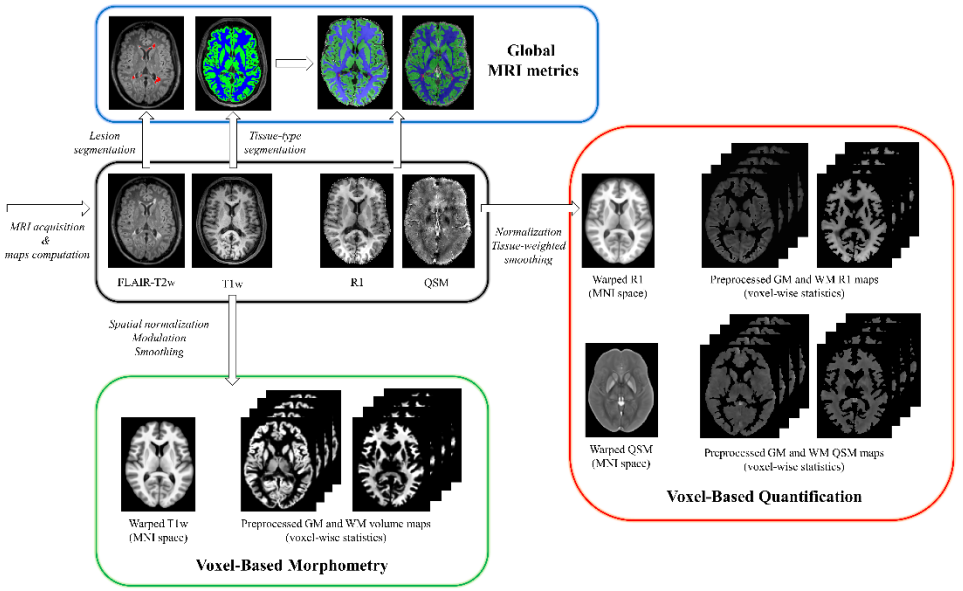

Figure 5.1. ***Workflow illustrating the main image processing and analysis steps.*** *Initially, quantitative maps were computed and mapped onto the corresponding T1-weighted volumes and demyelinating lesions were automatically segmented on FLAIR images. For voxel-based analyses, T1-weighted volumes were segmented into different tissue classes and normalized to a 1mm isotropic template in MNI space, with the estimated spatial transformations also applied to quantitative maps. Before entering voxel-wise statistical analyses, normalized gray matter and white matter probability maps were modulated and smoothed, while normalized R1 and χ maps were smoothed via a tissue-weighted smoothing procedure to account for the partial volume contribution of tissue density in each voxel. Using lesion and tissue class masks, global brain volumes and median values of R1 and χ in normal-appearing tissues were also obtained.*

Briefly, quantitative maps were mapped onto the corresponding T1-weighted volumes, demyelinating lesions were automatically segmented on FLAIR images via the Lesion Segmentation Tool (LST) toolbox (www.statistical-modelling.de/lst.html) and individual lesion probability maps were used to fill lesions in T1-weighted images and binarized to compute T2-LL.

Subsequent processing steps were carried out following the voxel-based morphometry (VBM)[44] and voxel-based quantification (VBQ)[133] approaches: filled T1-weighted volumes were segmented into different tissue classes and normalized to a 1mm isotropic template in MNI space via the standard pipeline implemented in the Computational Anatomy Toolbox (CAT12, http://neuro.uni-jena.de/cat), with the estimated spatial transformations also applied to quantitative maps. Finally, normalized GM and WM probability maps were modulated and smoothed using a 1mm full width at half maximum (FWHM) isotropic Gaussian kernel. Instead, normalized R1 and χ maps were smoothed (1-mm FWHM isotropic Gaussian kernel) via the tissue-weighted smoothing procedure implemented in the hMRI toolbox (https://hmri-group.github.io/hMRI-toolbox) to account for the partial volume contribution of tissue density in each voxel, resulting in tissue-specific smoothed quantitative maps in MNI space.

For each participant, total intracranial volume (TIV) was also estimated and brain parenchymal, GM and WM fractions (BPf, GMf, WMf) were computed. Additionally, individual normal-appearing GM and WM masks were obtained and used to extract median values of R1 and χ, while study-specific GM and WM masks were generated to restrict voxel-wise statistical comparisons in order to reduce possible spurious atrophy-related effects on VBQ analyses, as well as to ensure that each voxel was analyzed in only one subspace (i.e., GM or WM).

5.2.4 Statistical analysis

Unless otherwise specified, statistical analyses were carried out using the Statistical Package for Social Science (SPSSv25.0, IBM corp.) with a significance level α=0.05, and the Benjamini-Hochberg procedure was adopted for controlling the false discovery rate (FDR). Before running parametric analyses, assumptions of the linear model were preliminarily

verified.

Between-group differences were tested with either Student t (age), Pearson Chi-square (sex) or age- and sex-corrected ANCOVA (tissue volumes and median R1 and χ values) tests.

As for the VBM and VBQ analyses, normalized, modulated and smoothed tissue probability maps, as well as normalized and smoothed R1 and χ maps, were statistically analyzed, separately for GM and WM, to assess voxel-wise between-group differences using a nonparametric approach based on 5000 permutations applied to the general linear model[51] via the Threshold Free Cluster Enhancement (TFCE) toolbox (http://www.neuro.uni-jena.de/tfce). Age, sex and TIV were included in the model as confounding variables and previously generated explicit GM and WM masks were used, with a cluster extent threshold k=100 voxels and significance level $p<0.05$ after correction for multiple comparisons by controlling the family-wise error rate.

When significant between-group differences emerged at the voxel-based analyses, relationships between clinical variables (i.e. EDSS, SDMT and motor scores) and MRI metrics (tissue probability, R1, and χ maps) were assessed voxel-wise via the TFCE toolbox using regression models with individual clinical scores as the dependent variables and explicit masks restricting the analyses to areas of significant between-group differences. Robust partial correlation analyses, using bootstrap with 5000 resamples, were also carried out between clinical variables and global MRI metrics (i.e. T2-LL and tissue volumes and median R1 and χ values), correcting for age, sex and TIV (for volumes only).

5.3 Results

5.3.1 Subjects

117 MS patients (85 relapsing-remitting, 22 secondary-progressive, 10

primary-progressive; 40.6±11.9 years; F/M=85/32) were included in the study, along with 53 HS (41.3±11.6 years; F/M=33/20). Mean disease duration (DD) for MS patients was 12.7 years (SD: 8.3), with a median EDSS score of 3.0 (interquartile range: 2.0 - 5.25) and a mean T2-LL of 6.2 ml (SD: 10.7). 110 patients (94.0%) were under immunomodulatory treatment (32% with first line therapies: interferon, glatiramer acetate, dimethyl fumarate, teriflunomide; 62% with second line therapies: fingolimod, siponimod, natalizumab, alemtuzumab, ocrelizumab, cladribine) at the time of the MRI.

Demographic and clinical characteristics of the studied population, along with MRI-derived brain volumes and median R1 and χ values, are reported in Table 5.1.

	MS (*n*=117)	**HS (*n*=53)**	***p*-value*** (MS vs HC)**
Age (y)	40.6±11.9	41.3±11.6	0.71
*Female Sex**	85 (72.6%)	33 (62.3)	0.17
*DMT (first/second line/none)**	38/72/7 (32.5/61.5/6.0%)	-	-
*Disease Course (RR/SP/PP)**	85/22/10 (72.6/18.8/9.5%)	-	-
DD (y)	12.7±8.3	-	-
*EDSS***	3.0 (2.0 - 5.25)	-	-
Cognitive score	-0.82±1.16	-	
Motor score	-0.03±0.86	-	
T2-LL (ml)	6.2±10.7	-	-
BPf (%)	78.3±4.2	81.0±2.9	**<0.001**
GMf (%)	43.9±2.8	45.3±2.4	**<0.001**
WMf (%)	34.4±2.6	35.7±2.0	**<0.001**
NAGM median R1 (Hz)	0.66±0.06	0.70±0.06	**0.002**
NAWM median R1 (Hz)	0.99±0.09	1.06±0.09	**<0.001**
NAGM median χ (ppb)	2.84±1.81	2.44±1.67	0.19
NAWM median χ (ppb)	-9.47±2.58	-7.97±2.31	**<0.001**

Unless otherwise indicated, data are expressed as mean ± SD. Between-group differences were tested with either Student *t* (age), Pearson Chi-square (sex) or age- and sex-corrected ANCOVA (MRI-derived measures) tests.

* Data are the number of subjects, with percentages in parentheses.

** Data are medians, with interquartile ranges in parentheses.

*** Significant between-group differences are reported in bold.
Table 5.1. ***Demographic, clinical and MRI characteristics of the studied population.***

5.3.2 Between-group comparisons

Compared to HS, MS patients had lower GM, WM and whole-brain volume fractions (p-values≤0.001 for all), along with lower median NAGM R1 (p=0.002), NAWM R1 and χ (p ≤0.001) values.

At the voxel-based analyses (Figure 5.2), MS patients showed massive clusters of reduced volume compared to HC, extensively encompassing both supra- and infra-tentorial GM and WM, with local maxima located in the bilateral thalami and fornices, respectively (p-values <0.001).

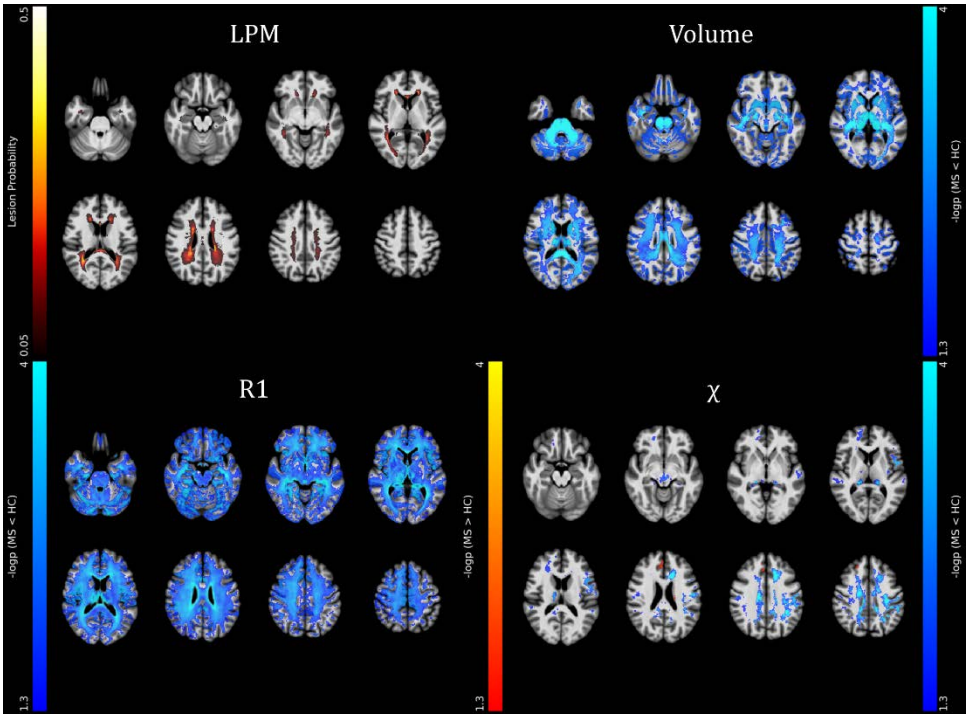

Figure 5.2. ***Results of the between-group voxel-wise comparisons.*** *A lesion probability map (LPM), obtained by summing all the binary lesion masks and dividing by the number of patients to give a lesion probability at each voxel, is presented (with a 5% probability threshold, upper left panel), along with clusters of significant between-group difference in terms of volume (upper right panel), R1 and χ (lower panels) values for both the MS>HC (red-yellow) and MS<HC*

(blue-light blue) contrasts, all superimposed on axial sections of the average T1-weighted volume in the MNI space. For Volume, R1 and χ maps, pooled results of the GM and WM analyses are shown. Images are in radiological orientation.

Similarly widespread clusters of reduced R1 values emerged in MS patients, extending well beyond the distribution of visible T2-hyperintense lesions and peaking in the corpus callosum, periventricular WM and thalami (p-values <0.001). As for the analysis of QSM images, MS patients showed several clusters of reduced χ values compared to HC, involving the bilateral cerebral WM (particularly the frontal sections of the corpus callosum, corona radiata, superior longitudinal fasciculus and cingulum - p-values <0.001), the midbrain (p=0.001), the bilateral pulvinar and right thalamic ventral lateral nucleus (p-values <0.001), along with small clusters of increased χ values in the left body of the caudate nucleus (p=0.004) and the right anterior cingulate (p=0.005) and superior frontal (p=0.02) gyri.

Effect size (Cohen's d) maps of between-group differences in terms of regional volume, R1 and χ values (obtained from permutation-based T statistics estimated in TFCE toolbox) are also presented in Figure 5.3.

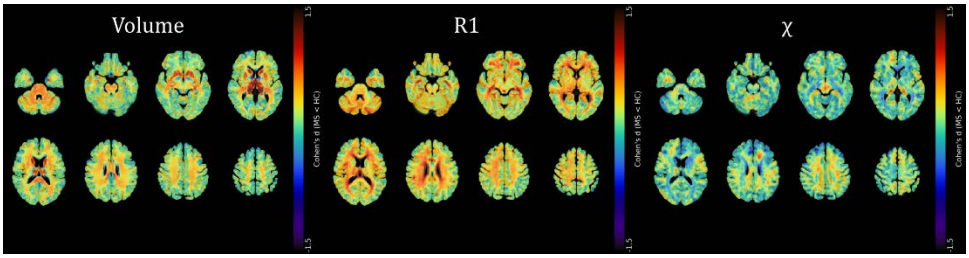

Figure 5.3. ***Effect size maps of between-group differences.*** *Effect size (Cohen's d) maps of between-group differences in terms of volume, R1 and χ values (from left to right) are presented, superimposed on axial sections of the average T1-weighted volume in the MNI space. Positive effect size values refer to the MS<HC contrast. For Volume, R1 and χ maps, pooled results of the GM and WM analyses are shown. Images are in radiological orientation.*

5.3.3 Relationship between MRI metrics and clinical status

When looking at the relationship with clinical variables, whole brain and

GM volumes were positively associated with motor performance (r=0.245, p=0.009 and r=0.241, p=0.01, respectively), with T2-LL and global GM volume correlating with cognitive processing speed (r=-0.255, p=0.006 and r=0.234, p=0.01, respectively) and more weakly with clinical disability (r=0.200, p=0.03 and r=-0.203, p=0.03, respectively, not surviving multiple comparisons correction). No significant correlations emerged between clinical status and median R1 and χ values of both NAGM and NAWM (Table 5.2).

	EDSS	**SDMT**	**Motor score**
Global MRI metrics[a]			
T2-LL	0.200 (0.033, 0.407) 0.03*	-0.255 (-0.360, -0.151) **0.006**	-0.164 (-0.324, -0.029) 0.09
Whole Brain volume	-0.161 (-0.356, 0.024) 0.09	0.177 (0.011, 0.339) 0.06	0.245 (0.078, 0.413) **0.009**
GM volume	-0.203 (-0.370, -0.027) 0.03*	0.234 (0.075, 0.386) **0.01**	0.241 (0.089, 0.381) **0.01**
WM volume	-0.061 (-0.246, 0.112) 0.52	0.057 (-0.158, 0.257) 0.55	0.153 (-0.016, 0.332) 0.11
NAGM median R1	-0.136 (-0.313, 0.053) 0.15	0.076 (-0.094, 0.250) 0.42	0.039 (-0.132, 0.210) 0.68
NAWM median R1	-0,158 (-0.331, 0.030) 0.10	0.167 (-0.009, 0.338) 0.08	0.118 (-0.042, 0.278) 0.22
NAGM median χ	0.007 (-0.187, 0.196) 0.94	-0.019 (-0.201, 0.167) 0.84	-0.022 (-0.224, 0.193) 0.82
NAWM median χ	-0.084 (-0.291, 0.140) 0.38	-0.030 (-0.200, 0.141) 0.75	0.136 (-0.049, 0.303) 0.15

Significant results are in bold.

[a] Correlations with clinical scores are corrected for age, sex and TIV (for volumes only).

* Not significant after FDR correction.

Table 5.2. ***Correlations between clinical and MRI-derived variables.*** *Results are expressed as correlation coefficients (r) with 95% bias-corrected and accelerated bootstrap confidence intervals in parentheses (first row) and corresponding p-values (second row).*

To allow for a precise anatomical localization of the effects of interest, associations with clinical variables were also tested at the voxel level (Figure 5.4): thalamic volume was related both negatively with clinical

disability (p=0.001) and positively with cognitive processing speed (p=0.001) and motor performance (p=0.01), with additional positive correlations between the SDMT score and GM volume in the right basal ganglia and posterior insula (p-values<0.04) and between motor performance and infratentorial WM volume at the level of the medial lemnisci and cerebellar peduncles (p=0.01). Furthermore, a large cluster of significant association between the SDMT score and R1 values emerged, extensively involving the (mainly posterior) periventricular WM and peaking around the right posterior thalamic radiation (p reaching 0.01), while χ values in the frontal sections of the cingulum and corona radiata were related both negatively with EDSS (p reaching <0.001) and positively with motor performance (p reaching 0.003).

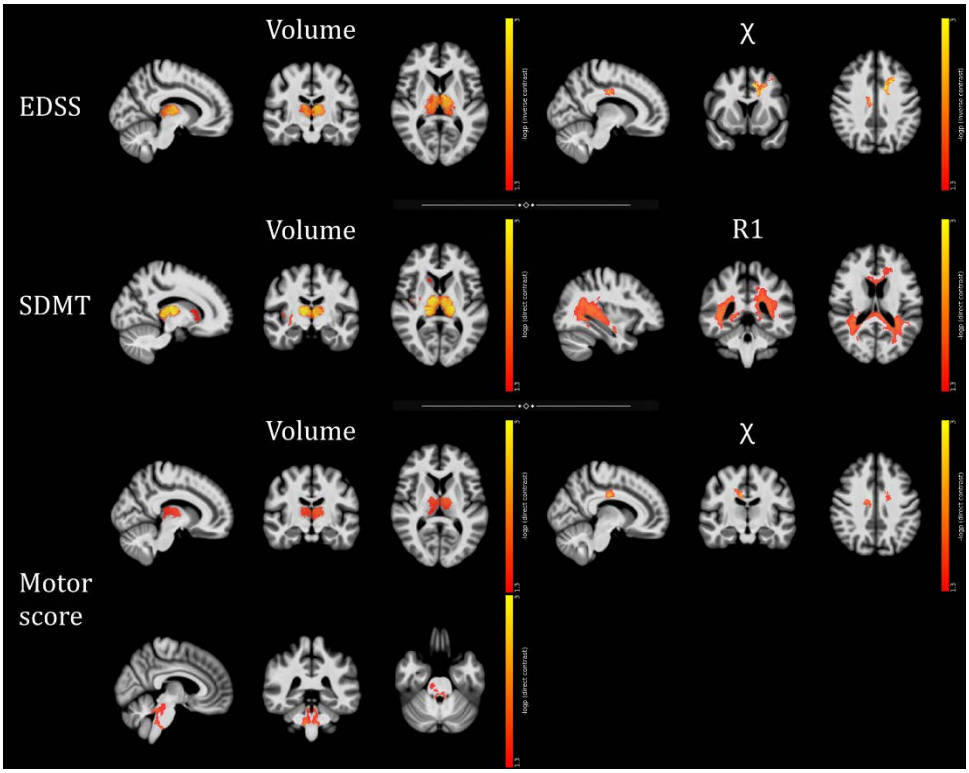

Figure 5.4. ***Results of the voxel-wise correlations with clinical variables.*** *Clusters of significant association between MRI metrics and EDSS, SDMT and motor (from top to bottom) scores are presented, superimposed on sagittal, coronal and axial (from left to right) sections of the average T1-weighted volume in the MNI space. Images are in radiological orientation.*

5.4 Discussion

Notwithstanding the many advances witnessed in the field of tissue microstructure in MS, none of the available MR techniques is solely affected by a specific pathological aspect, which advocates for the application of multi-parameter approaches to improve our understanding of microstructural damage.[134] Here, we applied a multi-parameter analysis of volumetry and quantitative MRI to address the following questions: (i) what is the topography of iron and myelin changes assessed via susceptibility and relaxometry in MS? and (ii) are the observed changes clinically relevant?

As per the first question, MS patients showed a widespread R1 decrease across GM and WM regions, associated to substantially more limited modifications in susceptibility and to an atrophy pattern mainly involving deep GM, posterior and infratentorial regions. The observed R1 reduction throughout the WM was likely driven by changes in macromolecular tissue content (i.e. myelin), and, to a lesser extent, by iron levels.[135] Indeed, pathological descriptions documented demyelination not only in the context of lesions, but also in normal-appearing WM,[136] with iron depletion in remyelinated plaques[118] also possibly contributing, to a lesser extent, to R1 reduction. The R1 voxel-wise analysis confirms and expands previous findings reporting R1 decrease in multiple WM tracts in MS compared to HS,[114] with no specific regional preference.[137] Similarly, the parallel susceptibility decrease in several WM regions confirms histopathological data reporting iron depletion in normal-appearing WM,[118] and adds on a recent study reporting a decrease in susceptibility within the cingulum in a relatively small group of patients.[138] Indeed, our larger sample size and the application of a voxel-wise approach likely explains the increased sensitivity to the detection of

between-group differences. Nevertheless, given previous histopathological data reporting significant decrease of iron in oligodendrocytes and myelin within normal-appearing WM,[117] the limited spatial extension of the observed susceptibility reduction is somehow surprising. A possible explanation could be that, as myelin and iron exert opposite effects on susceptibility, our ability to investigate tissues characterized by concomitant presence of demyelination and iron depletion remains intrinsically limited.

In GM, the observed R1 reduction was associated with decreased susceptibility in the thalamus and small clusters of increased susceptibility in the caudate nucleus and cortical areas. While R1 in the cortex and thalamus can be considered a reliable marker of myelin content,[139] in the basal ganglia it is highly influenced by iron concentration.[116] The observation that the thalamus undergoes structural modifications similar to those observed in WM, with demyelination associated with iron depletion, confirms recent findings[21,115,116,140] and can be explained by its peculiar anatomical structure. Likewise, our findings of small areas of increased susceptibility in the cortex and caudate nucleus are in line with recent reports, suggesting that susceptibility increase in MS deep GM, originally interpreted as demyelination and iron accrual,[121,124] is mainly accounted for by atrophy rather than actual increase in iron content.[115,116]

As per the clinical meaning of microstructural abnormalities, R1 changes seem to reflect the impact of focal lesions, with the cluster holding significant correlation with cognitive performance peaking in the periventricular region, in overlap with focal demyelination, likely causing disconnection of distributed networks responsible for the control of high-level functions. On the other hand, susceptibility and atrophy, reflecting oligodendrocyte and axonal damage, significantly contributed to global and motor disability. Our analysis confirmed not only the central role of

thalamic atrophy as meaningful correlate of disability in MS,[28] but also the relevance of cerebellar WM damage in driving motor impairment.[141] Beyond these confirmations, we identified a correlation between susceptibility reduction and disability that might add another layer to our understanding of the pathological mechanisms sustaining clinical impairment in MS. Indeed, if susceptibility decrease is expression of oligodendrocyte damage,[117] the consequent reduction of the tissue repair capability, depending upon oligodendrocyte activity, would contribute to the manifestation of clinical deficits. On the other hand, cognitive performance was related to deep GM atrophy and R1 abnormalities mostly overlapping the distribution of focal WM lesions. Such overlap, together with the correlation identified between lesion load and SDMT, suggests that, rather than microstructural damage, GM atrophy and disconnection sustained by focal lesions remain the main predictors of cognitive dysfunction in MS.[142]

Our work is not without limitations. First, our assessment was conducted on the entire GM and WM rather than the normal-appearing tissue. However, when comparing extra-lesional median R1/susceptibility values at group level, we identified significant differences, demonstrating that microstructural abnormalities also affect normal-appearing tissue. Additionally, the voxel-based analysis clearly demonstrated that such modifications are not spatially restricted to areas affected by T2 hyperintense lesions, as R1/susceptibility alterations are not only present where lesion have higher probability to occur, but are also identified within normal-appearing tissue. Finally, although our clinical evaluation included motor and cognitive assessments, and our approach allowed for a multifaceted exploration of tissue abnormalities, we are still far from a comprehensive characterization of the structural substrate underpinning clinical disability in MS.

In conclusion, we confirmed the presence of widespread and clinically

relevant demyelination, expressed by R1 decrease, and atrophy in MS. In addition, our findings suggest that also the more limited modifications of tissue susceptibility are clinically meaningful, possibly adding information on oligodendrocyte dysfunction and damage to the ones provided by demyelination and atrophy estimation.

Bibliography

1. Jenkinson M, Chappell M. *Introduction to Neuroimaging Analysis*. First edition. Oxford University Press; 2018.

2. Erickson BJ, Korfiatis P, Akkus Z, Kline TL. Machine Learning for Medical Imaging. *RadioGraphics*. Published online February 17, 2017. doi:10.1148/rg.2017160130

3. Filippi M, Brück W, Chard D, et al. Association between pathological and MRI findings in multiple sclerosis. *The Lancet Neurology*. 2019;18(2):198-210. doi:10.1016/s1474-4422(18)30451-4

4. Vermersch P, Berger T, Gold R, et al. The clinical perspective: How to personalise treatment in MS and how may biomarkers including imaging contribute to this? *Multiple sclerosis (Houndmills, Basingstoke, England)*. 2016;22(2 Suppl):18-33. doi:10.1177/1352458516650739

5. Traboulsee A, Simon JH, Stone L, et al. Revised Recommendations of the Consortium of MS Centers Task Force for a Standardized MRI Protocol and Clinical Guidelines for the Diagnosis and Follow-Up of Multiple Sclerosis. *AJNR American journal of neuroradiology*. 2016;37(3):394-401. doi:10.3174/ajnr.A4539

6. Wattjes MP, Rovira A, Miller D, et al. Evidence-based guidelines: MAGNIMS consensus guidelines on the use of MRI in multiple sclerosis--establishing disease prognosis and monitoring patients. *Nature reviews Neurology*. 2015;11(10):597-606. doi:10.1038/nrneurol.2015.157

7. Pontillo G, Cocozza S, Di Stasi M, et al. 2D linear measures of ventricular enlargement may be relevant markers of brain atrophy and long-term disability progression in multiple sclerosis. *European radiology*. 2020;30(7):3813-3822. doi:10.1007/s00330-020-06738-4

8. Young AL, Marinescu RV, Oxtoby NP, et al. Uncovering the heterogeneity and temporal complexity of neurodegenerative diseases with Subtype and Stage Inference. *Nature communications*. 2018;9(1):4273. doi:10.1038/s41467-018-05892-0

9. Fonteijn HM, Modat M, Clarkson MJ, et al. An event-based model for disease progression and its application in familial Alzheimer's disease and Huntington's disease. *NeuroImage*. 2012;60(3):1880-1889. doi:10.1016/j.neuroimage.2012.01.062

10. Eshaghi A, Marinescu RV, Young AL, et al. Progression of regional grey matter atrophy in multiple sclerosis. *Brain : a journal of neurology*. 2018;141(6):1665-1677. doi:10.1093/brain/awy088

11. Dekker I, Schoonheim MM, Venkatraghavan V, et al. The sequence of structural, functional and cognitive changes in multiple sclerosis. *NeuroImage Clinical*. 2021;29:102550. doi:10.1016/j.nicl.2020.102550

12. Eshaghi A, Young AL, Wijeratne PA, et al. Identifying multiple sclerosis subtypes using unsupervised machine learning and MRI data. *Nat Commun*. 2021;12(1):2078. doi:10.1038/s41467-021-22265-2

13. Polman CH, Reingold SC, Banwell B, et al. Diagnostic criteria for multiple sclerosis: 2010 revisions to the McDonald criteria. *Ann Neurol*. 2011;69(2):292-302. doi:10.1002/ana.22366

14. Lublin FD. New multiple sclerosis phenotypic classification. *Eur Neurol*. 2014;72 Suppl 1:1-5. doi:10.1159/000367614

15. Confavreux C, Vukusic S. Age at disability milestones in multiple sclerosis. *Brain : a journal of neurology*. 2006;129(Pt 3):595-605. doi:10.1093/brain/awh714

16. Goretti B, Niccolai C, Hakiki B, et al. The Brief International Cognitive Assessment for Multiple Sclerosis (BICAMS): normative values with gender, age and education corrections in the Italian population. *BMC neurology*. 2014;14:171. doi:10.1186/s12883-014-0171-6

17. Benedict RH, Amato MP, Boringa J, et al. Brief International Cognitive Assessment for MS (BICAMS): international standards for validation. *BMC Neurol*. 2012;12(1):55. doi:10.1186/1471-2377-12-55

18. Tzourio-Mazoyer N, Landeau B, Papathanassiou D, et al. Automated anatomical labeling of activations in SPM using a macroscopic anatomical parcellation of the MNI MRI single-subject brain. *NeuroImage*. 2002;15(1):273-289. doi:10.1006/nimg.2001.0978

19. Hayes AF, Krippendorff K. Answering the Call for a Standard Reliability Measure for Coding Data. *Communication Methods and Measures*. 2007;1(1):77-89. doi:10.1080/19312450709336664

20. Gibbs RM, Lipnick S, Bateman JW, et al. Toward Precision Medicine for Neurological and Neuropsychiatric Disorders. *Cell stem cell*. 2018;23(1):21-24. doi:10.1016/j.stem.2018.05.019

21. Pontillo G, Cocozza S, Lanzillo R, et al. Determinants of Deep Gray Matter Atrophy in Multiple Sclerosis: A Multimodal MRI Study. *AJNR American journal of neuroradiology*. 2019;40(1):99-106. doi:10.3174/ajnr.A5915

22. Calabrese M, Magliozzi R, Ciccarelli O, Geurts JJG, Reynolds R, Martin R. Exploring the origins of grey matter damage in multiple sclerosis. *Nature Reviews Neuroscience*. 2015;16(3):147-158. doi:10.1038/nrn3900

23. Geurts JJ, Barkhof F. Grey matter pathology in multiple sclerosis. *The Lancet Neurology*. 2008;7(9):841-851. doi:10.1016/s1474-4422(08)70191-1

24. Ruggieri S, Petracca M, Miller A, et al. Association of Deep Gray Matter Damage With Cortical and Spinal Cord Degeneration in Primary Progressive Multiple Sclerosis. *JAMA neurology*. 2015;72(12):1466-1474. doi:10.1001/jamaneurol.2015.1897

25. Wijnands JMA, Kingwell E, Zhu F, et al. Health-care use before a first demyelinating event suggestive of a multiple sclerosis prodrome: a matched cohort study. *The Lancet Neurology*. 2017;16(6):445-451. doi:10.1016/s1474-4422(17)30076-5

26. Pagani E, Rocca MA, Gallo A, et al. Regional brain atrophy evolves differently in patients with multiple sclerosis according to clinical phenotype. *AJNR American journal of neuroradiology*. 2005;26(2):341-346.

27. Fisher E, Lee JC, Nakamura K, Rudick RA. Gray matter atrophy in multiple sclerosis: a longitudinal study. *Annals of neurology*. 2008;64(3):255-265. doi:10.1002/ana.21436

28. Eshaghi A, Prados F, Brownlee WJ, et al. Deep gray matter volume loss drives disability worsening in multiple sclerosis: Deep Gray Matter Volume Loss. *Ann Neurol*. 2018;83(2):210-222. doi:10.1002/ana.25145

29. Minagar A, Barnett MH, Benedict RH, et al. The thalamus and multiple sclerosis: modern views on pathologic, imaging, and clinical aspects. *Neurology*. 2013;80(2):210-219. doi:10.1212/WNL.0b013e31827b910b

30. Houtchens MK, Benedict RH, Killiany R, et al. Thalamic atrophy and cognition in multiple sclerosis. *Neurology*. 2007;69(12):1213-1223.

doi:10.1212/01.wnl.0000276992.17011.b5

31. Petracca M, Pontillo G, Moccia M, et al. Neuroimaging Correlates of Cognitive Dysfunction in Adults with Multiple Sclerosis. *Brain sciences*. 2021;11(3). doi:10.3390/brainsci11030346

32. Cocozza S, Pontillo G, Russo C, et al. Cerebellum and cognition in progressive MS patients: functional changes beyond atrophy? *Journal of neurology*. 2018;265(10):2260-2266. doi:10.1007/s00415-018-8985-6

33. Germain DP. Fabry disease. *Orphanet Journal of Rare Diseases*. 2010;5(1):30. doi:10.1186/1750-1172-5-30

34. Kolodny E, Fellgiebel A, Hilz MJ, et al. Cerebrovascular involvement in Fabry disease: current status of knowledge. *Stroke*. 2015;46(1):302-313. doi:10.1161/STROKEAHA.114.006283

35. Cocozza S, Russo C, Pontillo G, Pisani A, Brunetti A. Neuroimaging in Fabry disease: current knowledge and future directions. *Insights Imaging*. 2018;9(6):1077-1088. doi:10.1007/s13244-018-0664-8

36. Azevedo O, Cordeiro F, Gago MF, et al. Fabry Disease and the Heart: A Comprehensive Review. *Int J Mol Sci*. 2021;22(9):4434. doi:10.3390/ijms22094434

37. Cole JH, Franke K. Predicting Age Using Neuroimaging: Innovative Brain Ageing Biomarkers. *Trends Neurosci*. 2017;40(12):681-690. doi:10.1016/j.tins.2017.10.001

38. Kaufmann T, van der Meer D, Doan NT, et al. Common brain disorders are associated with heritable patterns of apparent aging of the brain. *Nat Neurosci*. 2019;22(10):1617-1623. doi:10.1038/s41593-019-0471-7

39. Wagen AZ, Coath W, Keshavan A, et al. Life course, genetic, and neuropathological associations with brain age in the 1946 British Birth Cohort: a population-based study. *Lancet Healthy Longev*. 2022;3(9):e607-e616. doi:10.1016/S2666-7568(22)00167-2

40. Shi Y, Mao H, Gao Q, et al. Potential of brain age in identifying early cognitive impairment in subcortical small-vessel disease patients. *Front Aging Neurosci*. 2022;14:973054. doi:10.3389/fnagi.2022.973054

41. Lee PL, Kuo CY, Wang PN, et al. Regional rather than global brain age mediates cognitive function in cerebral small vessel disease. *Brain*

Communications. 2022;4(5):fcac233. doi:10.1093/braincomms/fcac233

42. Vardarli I, Rischpler C, Herrmann K, Weidemann F. Diagnosis and Screening of Patients with Fabry Disease. *Ther Clin Risk Manag*. 2020;16:551-558. doi:10.2147/TCRM.S247814

43. Mignani R, Pieruzzi F, Berri F, et al. FAbry STabilization indEX (FASTEX): an innovative tool for the assessment of clinical stabilization in Fabry disease. *Clin Kidney J*. 2016;9(5):739-747. doi:10.1093/ckj/sfw082

44. Ashburner J, Friston KJ. Voxel-based morphometry--the methods. *Neuroimage*. 2000;11(6 Pt 1):805-821. doi:10.1006/nimg.2000.0582

45. Tustison NJ, Avants BB, Cook PA, et al. N4ITK: Improved N3 Bias Correction. *IEEE Transactions on Medical Imaging*. 2010;29(6):1310-1320. doi:10.1109/TMI.2010.2046908

46. Huang G, Liu Z, van der Maaten L, Weinberger KQ. Densely Connected Convolutional Networks. In: ; 2017:4700-4708. Accessed October 31, 2022. https://openaccess.thecvf.com/content_cvpr_2017/html/Huang_Densely_Connected_Convolutional_CVPR_2017_paper.html

47. He K, Zhang X, Ren S, Sun J. Deep Residual Learning for Image Recognition. In: ; 2016:770-778. Accessed October 31, 2022. https://openaccess.thecvf.com/content_cvpr_2016/html/He_Deep_Residual_Learning_CVPR_2016_paper.html

48. Paszke A, Gross S, Massa F, et al. PyTorch: An Imperative Style, High-Performance Deep Learning Library. In: *Advances in Neural Information Processing Systems*. Vol 32. Curran Associates, Inc.; 2019. Accessed October 31, 2022. https://proceedings.neurips.cc/paper/2019/hash/bdbca288fee7f92f2bfa9f7012727740-Abstract.html

49. Chen LC, Papandreou G, Kokkinos I, Murphy K, Yuille AL. DeepLab: Semantic Image Segmentation with Deep Convolutional Nets, Atrous Convolution, and Fully Connected CRFs. *IEEE Transactions on Pattern Analysis and Machine Intelligence*. 2018;40(4):834-848. doi:10.1109/TPAMI.2017.2699184

50. de Lange AMG, Kaufmann T, van der Meer D, et al. Population-based neuroimaging reveals traces of childbirth in the maternal brain. *Proc Natl Acad Sci U S A*. 2019;116(44):22341-22346.

doi:10.1073/pnas.1910666116

51. Winkler AM, Ridgway GR, Webster MA, Smith SM, Nichols TE. Permutation inference for the general linear model. *Neuroimage*. 2014;92:381-397. doi:10.1016/j.neuroimage.2014.01.060

52. Wood DA, Kafiabadi S, Busaidi AA, et al. Accurate brain-age models for routine clinical MRI examinations. *Neuroimage*. 2022;249:118871. doi:10.1016/j.neuroimage.2022.118871

53. Leonardsen EH, Peng H, Kaufmann T, et al. Deep neural networks learn general and clinically relevant representations of the ageing brain. *Neuroimage*. 2022;256:119210. doi:10.1016/j.neuroimage.2022.119210

54. Burns JC, Cotleur B, Walther DM, et al. Differential accumulation of storage bodies with aging defines discrete subsets of microglia in the healthy brain. *Elife*. 2020;9:e57495. doi:10.7554/eLife.57495

55. Pontillo G, Cocozza S, Brunetti A, et al. Reduced Intracranial Volume in Fabry Disease: Evidence of Abnormal Neurodevelopment? *Front Neurol*. 2018;9:672. doi:10.3389/fneur.2018.00672

56. Vidal-Pineiro D, Wang Y, Krogsrud SK, et al. Individual variations in "brain age" relate to early-life factors more than to longitudinal brain change. *Elife*. 2021;10:e69995. doi:10.7554/eLife.69995

57. Cocozza S, Pontillo G, Quarantelli M, et al. Default mode network modifications in Fabry disease: A resting-state fMRI study with structural correlations. *Hum Brain Mapp*. 2018;39(4):1755-1764. doi:10.1002/hbm.23949

58. Cole JH, Marioni RE, Harris SE, Deary IJ. Brain age and other bodily "ages": implications for neuropsychiatry. *Mol Psychiatry*. 2019;24(2):266-281. doi:10.1038/s41380-018-0098-1

59. Tian YE, Cropley V, Maier AB, Lautenschlager NT, Breakspear M, Zalesky A. Biological aging of human body and brain systems. Published online September 4, 2022:2022.09.03.22279337. doi:10.1101/2022.09.03.22279337

60. McCutcheon RA, Reis Marques T, Howes OD. Schizophrenia-An Overview. *JAMA Psychiatry*. 2020;77(2):201-210. doi:10.1001/jamapsychiatry.2019.3360

61. Keefe RSE, Harvey PD. Cognitive impairment in schizophrenia.

In: *Novel Antischizophrenia Treatments*. Handbook of experimental pharmacology. Springer Science + Business Media; 2012:11-37. doi:10.1007/978-3-642-25758-2_2

62. Toulopoulouand T, Murray RM. Verbal memory deficit in patients with schizophrenia: an important future target for treatment. *Expert Rev Neurother*. 2004;4(1):43-52. doi:10.1586/14737175.4.1.43

63. Francis A, Seidman L, Tandon N, et al. Reduced subicular subdivisions of the hippocampal formation and verbal declarative memory impairments in young relatives at risk for schizophrenia. *Schizophr Res*. 2013;151(1-3). doi:10.1016/j.schres.2013.10.002

64. Guimond S, Chakravarty MM, Bergeron-Gagnon L, Patel R, Lepage M. Verbal memory impairments in schizophrenia associated with cortical thinning. *Neuroimage Clin*. 2016;11:20-29. doi:10.1016/j.nicl.2015.12.010

65. Borgan F, O'Daly O, Veronese M, et al. The neural and molecular basis of working memory function in psychosis: a multimodal PET-fMRI study. *Mol Psychiatry*. 2021;26(8):4464-4474. doi:10.1038/s41380-019-0619-6

66. Fox MD. Mapping Symptoms to Brain Networks with the Human Connectome. *N Engl J Med*. 2018;379(23):2237-2245. doi:10.1056/NEJMra1706158

67. Friston K, Brown HR, Siemerkus J, Stephan KE. The dysconnection hypothesis (2016). *Schizophrenia Research*. 2016;176(2-3):83-94. doi:10.1016/j.schres.2016.07.014

68. Wheeler AL, Voineskos AN. A review of structural neuroimaging in schizophrenia: from connectivity to connectomics. *Front Hum Neurosci*. 2014;8. doi:10.3389/fnhum.2014.00653

69. Dong D, Wang Y, Chang X, Luo C, Yao D. Dysfunction of Large-Scale Brain Networks in Schizophrenia: A Meta-analysis of Resting-State Functional Connectivity. *Schizophr Bull*. 2018;44(1):168-181. doi:10.1093/schbul/sbx034

70. Kraguljac NV, McDonald WM, Widge AS, Rodriguez CI, Tohen M, Nemeroff CB. Neuroimaging Biomarkers in Schizophrenia. *Am J Psychiatry*. 2021;178(6):509-521. doi:10.1176/appi.ajp.2020.20030340

71. Voineskos AN, Jacobs GR, Ameis SH. Neuroimaging Heterogeneity in Psychosis: Neurobiological Underpinnings and

Opportunities for Prognostic and Therapeutic Innovation. *Biol Psychiatry*. 2020;88(1):95-102. doi:10.1016/j.biopsych.2019.09.004

72. Calhoun VD, Sui J. Multimodal Fusion of Brain Imaging Data: A Key to Finding the Missing Link(s) in Complex Mental Illness. *Biological Psychiatry: Cognitive Neuroscience and Neuroimaging*. 2016;1(3):230-244. doi:10.1016/j.bpsc.2015.12.005

73. Gardner DM, Murphy AL, O'Donnell H, Centorrino F, Baldessarini RJ. International consensus study of antipsychotic dosing. *Am J Psychiatry*. 2010;167(6):686-693. doi:10.1176/appi.ajp.2009.09060802

74. Kay SR, Fiszbein A, Opler LA. The positive and negative syndrome scale (PANSS) for schizophrenia. *Schizophr Bull*. 1987;13(2):261-276. doi:10.1093/schbul/13.2.261

75. Anselmetti S, Poletti S, Ermoli E, et al. The Brief Assessment of Cognition in Schizophrenia. Normative data for the Italian population. *Neurol Sci*. 2008;29(2):85-92. doi:10.1007/s10072-008-0866-9

76. Schaefer A, Kong R, Gordon EM, et al. Local-Global Parcellation of the Human Cerebral Cortex from Intrinsic Functional Connectivity MRI. *Cereb Cortex*. 2018;28(9):3095-3114. doi:10.1093/cercor/bhx179

77. Tian Y, Margulies DS, Breakspear M, Zalesky A. Topographic organization of the human subcortex unveiled with functional connectivity gradients. *Nat Neurosci*. 2020;23(11):1421-1432. doi:10.1038/s41593-020-00711-6

78. Thomas Yeo BT, Krienen FM, Sepulcre J, et al. The organization of the human cerebral cortex estimated by intrinsic functional connectivity. *J Neurophysiol*. 2011;106(3):1125-1165. doi:10.1152/jn.00338.2011

79. Cieslak M, Cook PA, He X, et al. QSIPrep: an integrative platform for preprocessing and reconstructing diffusion MRI data. *Nat Methods*. 2021;18(7):775-778. doi:10.1038/s41592-021-01185-5

80. Esteban O, Markiewicz CJ, Blair RW, et al. fMRIPrep: a robust preprocessing pipeline for functional MRI. *Nat Methods*. 2019;16(1):111-116. doi:10.1038/s41592-018-0235-4

81. Mandke K, Meier J, Brookes MJ, et al. Comparing multilayer brain networks between groups: Introducing graph metrics and recommendations. *NeuroImage*. 2018;166:371-384.

doi:10.1016/j.neuroimage.2017.11.016

82. Baggio HC, Abos A, Segura B, et al. Statistical inference in brain graphs using threshold-free network-based statistics. *Hum Brain Mapp*. 2018;39(6):2289-2302. doi:10.1002/hbm.24007

83. Zalesky A, Fornito A, Bullmore ET. Network-based statistic: Identifying differences in brain networks. *NeuroImage*. 2010;53(4):1197-1207. doi:10.1016/j.neuroimage.2010.06.041

84. Smith SM, Nichols TE. Threshold-free cluster enhancement: addressing problems of smoothing, threshold dependence and localisation in cluster inference. *Neuroimage*. 2009;44(1):83-98. doi:10.1016/j.neuroimage.2008.03.061

85. Amico E, Goñi J. Mapping hybrid functional-structural connectivity traits in the human connectome. *Network Neuroscience*. 2018;2(3):306-322. doi:10.1162/netn_a_00049

86. Canu E, Agosta F, Filippi M. A selective review of structural connectivity abnormalities of schizophrenic patients at different stages of the disease. *Schizophrenia Research*. 2015;161(1):19-28. doi:10.1016/j.schres.2014.05.020

87. Goldman SA. Glial evolution as a determinant of human behavior and its disorders. *Ann NY Acad Sci*. 2020;1471(1):72-85. doi:10.1111/nyas.14372

88. Liu SH, Du Y, Chen L, Cheng Y. Glial Cell Abnormalities in Major Psychiatric Diseases: A Systematic Review of Postmortem Brain Studies. *Mol Neurobiol*. 2022;59(3):1665-1692. doi:10.1007/s12035-021-02672-8

89. Alves PN, Foulon C, Karolis V, et al. An improved neuroanatomical model of the default-mode network reconciles previous neuroimaging and neuropathological findings. *Commun Biol*. 2019;2:370. doi:10.1038/s42003-019-0611-3

90. Hu ML, Zong XF, Mann JJ, et al. A Review of the Functional and Anatomical Default Mode Network in Schizophrenia. *Neurosci Bull*. 2017;33(1):73-84. doi:10.1007/s12264-016-0090-1

91. Camchong J, MacDonald AW, Bell C, Mueller BA, Lim KO. Altered functional and anatomical connectivity in schizophrenia. *Schizophr Bull*. 2011;37(3):640-650. doi:10.1093/schbul/sbp131

92. Ćurčić-Blake B, van der Meer L, Pijnenborg GHM, David AS, Aleman A. Insight and psychosis: Functional and anatomical brain connectivity and self-reflection in Schizophrenia. *Hum Brain Mapp*. 2015;36(12):4859-4868. doi:10.1002/hbm.22955

93. Supekar K, Uddin LQ, Prater K, Amin H, Greicius MD, Menon V. Development of functional and structural connectivity within the default mode network in young children. *NeuroImage*. 2010;52(1):290-301. doi:10.1016/j.neuroimage.2010.04.009

94. Giraldo-Chica M, Rogers BP, Damon SM, Landman BA, Woodward ND. Prefrontal-Thalamic Anatomical Connectivity and Executive Cognitive Function in Schizophrenia. *Biological Psychiatry*. 2018;83(6):509-517. doi:10.1016/j.biopsych.2017.09.022

95. Sheffield JM, Huang AS, Rogers BP, et al. Thalamocortical Anatomical Connectivity in Schizophrenia and Psychotic Bipolar Disorder. *Schizophrenia Bulletin*. 2020;46(5):1062-1071. doi:10.1093/schbul/sbaa022

96. Yao B, Neggers SFW, Kahn RS, Thakkar KN. Altered thalamocortical structural connectivity in persons with schizophrenia and healthy siblings. *NeuroImage: Clinical*. 2020;28:102370. doi:10.1016/j.nicl.2020.102370

97. Bracht T, Viher PV, Stegmayer K, et al. Increased structural connectivity of the medial forebrain bundle in schizophrenia spectrum disorders is associated with delusions of paranoid threat and grandiosity. *NeuroImage: Clinical*. 2019;24:102044. doi:10.1016/j.nicl.2019.102044

98. Yamamoto M, Kushima I, Suzuki R, et al. Aberrant functional connectivity between the thalamus and visual cortex is related to attentional impairment in schizophrenia. *Psychiatry Research: Neuroimaging*. 2018;278:35-41. doi:10.1016/j.pscychresns.2018.06.007

99. Clinton SM, Meador-Woodruff JH. Thalamic dysfunction in schizophrenia: neurochemical, neuropathological, and in vivo imaging abnormalities. *Schizophrenia Research*. 2004;69(2-3):237-253. doi:10.1016/j.schres.2003.09.017

100. Hwang K, Bertolero MA, Liu WB, D'Esposito M. The Human Thalamus Is an Integrative Hub for Functional Brain Networks. *The Journal of neuroscience : the official journal of the Society for Neuroscience*. 2017;37(23):5594-5607. doi:10.1523/JNEUROSCI.0067-17.2017

101. Kaufmann T, Skåtun KC, Alnæs D, et al. Disintegration of Sensorimotor Brain Networks in Schizophrenia. *Schizophr Bull*. 2015;41(6):1326-1335. doi:10.1093/schbul/sbv060

102. Bordier C, Nicolini C, Forcellini G, Bifone A. Disrupted modular organization of primary sensory brain areas in schizophrenia. *NeuroImage: Clinical*. 2018;18:682-693. doi:10.1016/j.nicl.2018.02.035

103. Walther S. Psychomotor symptoms of schizophrenia map on the cerebral motor circuit. *Psychiatry Res*. 2015;233(3):293-298. doi:10.1016/j.pscychresns.2015.06.010

104. Seitzman BA, Snyder AZ, Leuthardt EC, Shimony JS. The State of Resting State Networks. *Topics in Magnetic Resonance Imaging*. 2019;28(4):189-196. doi:10.1097/RMR.0000000000000214

105. Cole MW, Anticevic A, Repovs G, Barch D. Variable Global Dysconnectivity and Individual Differences in Schizophrenia. *Biological Psychiatry*. 2011;70(1):43-50. doi:10.1016/j.biopsych.2011.02.010

106. Fair DA, Cohen AL, Power JD, et al. Functional Brain Networks Develop from a "Local to Distributed" Organization. Sporns O, ed. *PLoS Comput Biol*. 2009;5(5):e1000381. doi:10.1371/journal.pcbi.1000381

107. Lefebvre S, Very E, Jardri R, et al. The neural correlates of the visual consciousness in schizophrenia: an fMRI study. *Eur Arch Psychiatry Clin Neurosci*. 2021;271(4):661-675. doi:10.1007/s00406-020-01167-2

108. Dima D, Roiser JP, Dietrich DE, et al. Understanding why patients with schizophrenia do not perceive the hollow-mask illusion using dynamic causal modelling. *NeuroImage*. 2009;46(4):1180-1186. doi:10.1016/j.neuroimage.2009.03.033

109. Dixon ML, De La Vega A, Mills C, et al. Heterogeneity within the frontoparietal control network and its relationship to the default and dorsal attention networks. *Proc Natl Acad Sci USA*. 2018;115(7). doi:10.1073/pnas.1715766115

110. Javitt DC. Sensory Processing in Schizophrenia: Neither Simple nor Intact. *Schizophrenia Bulletin*. 2009;35(6):1059-1064. doi:10.1093/schbul/sbp110

111. Javitt DC. When doors of perception close: bottom-up models of disrupted cognition in schizophrenia. *Annu Rev Clin Psychol*. 2009;5:249-275. doi:10.1146/annurev.clinpsy.032408.153502

112. Does MD. Inferring brain tissue composition and microstructure via MR relaxometry. *Neuroimage*. 2018;182:136-148. doi:10.1016/j.neuroimage.2017.12.087

113. Stuber C, Pitt D, Wang Y. Iron in Multiple Sclerosis and Its Noninvasive Imaging with Quantitative Susceptibility Mapping. *Int J Mol Sci*. 2016;17(1). doi:10.3390/ijms17010100

114. O'Muircheartaigh J, Vavasour I, Ljungberg E, et al. Quantitative neuroimaging measures of myelin in the healthy brain and in multiple sclerosis. *Hum Brain Mapp*. 2019;40(7):2104-2116. doi:10.1002/hbm.24510

115. Schweser F, Hagemeier J, Dwyer MG, et al. Decreasing brain iron in multiple sclerosis: The difference between concentration and content in iron MRI. *Human brain mapping*. 2021;42(5):1463-1474. doi:10.1002/hbm.25306

116. Pontillo G, Petracca M, Monti S, et al. Unraveling Deep Gray Matter Atrophy and Iron and Myelin Changes in Multiple Sclerosis. *AJNR American journal of neuroradiology*. Published online April 22, 2021. doi:10.3174/ajnr.A7093

117. Hametner S, Wimmer I, Haider L, Pfeifenbring S, Bruck W, Lassmann H. Iron and neurodegeneration in the multiple sclerosis brain. *Ann Neurol*. 2013;74(6):848-861. doi:10.1002/ana.23974

118. Hametner S, Endmayr V, Deistung A, et al. The influence of brain iron and myelin on magnetic susceptibility and effective transverse relaxation - A biochemical and histological validation study. *Neuroimage*. 2018;179:117-133. doi:10.1016/j.neuroimage.2018.06.007

119. Mottershead JP, Schmierer K, Clemence M, et al. High field MRI correlates of myelin content and axonal density in multiple sclerosis--a post-mortem study of the spinal cord. *J Neurol*. 2003;250(11):1293-1301. doi:10.1007/s00415-003-0192-3

120. Schmierer K, Wheeler-Kingshott CAM, Tozer DJ, et al. Quantitative magnetic resonance of postmortem multiple sclerosis brain before and after fixation. *Magnetic resonance in medicine*. 2008;59(2):268-277. doi:https://doi.org/10.1002/mrm.21487

121. Rudko DA, Solovey I, Gati JS, Kremenchutzky M, Menon RS. Multiple sclerosis: improved identification of disease-relevant changes in gray and white matter by using susceptibility-based MR imaging.

Radiology. 2014;272(3):851-864. doi:10.1148/radiol.14132475

122. Zivadinov R, Heininen-Brown M, Schirda CV, et al. Abnormal subcortical deep-gray matter susceptibility-weighted imaging filtered phase measurements in patients with multiple sclerosis: a case-control study. *Neuroimage*. 2012;59(1):331-339. doi:10.1016/j.neuroimage.2011.07.045

123. Schmalbrock P, Prakash RS, Schirda B, et al. Basal Ganglia Iron in Patients with Multiple Sclerosis Measured with 7T Quantitative Susceptibility Mapping Correlates with Inhibitory Control. *AJNR Am J Neuroradiol*. 2016;37(3):439-446. doi:10.3174/ajnr.A4599

124. Fujiwara E, Kmech JA, Cobzas D, et al. Cognitive Implications of Deep Gray Matter Iron in Multiple Sclerosis. *AJNR Am J Neuroradiol*. 2017;38(5):942-948. doi:10.3174/ajnr.A5109

125. Hernandez-Torres E, Wiggermann V, Machan L, et al. Increased mean R2* in the deep gray matter of multiple sclerosis patients: Have we been measuring atrophy? *J Magn Reson Imaging*. 2019;50(1):201-208. doi:10.1002/jmri.26561

126. Kurtzke JF. Rating neurologic impairment in multiple sclerosis: an expanded disability status scale (EDSS). *Neurology*. 1983;33(11):1444-1452. doi:10.1212/wnl.33.11.1444

127. Fischer JS, Rudick RA, Cutter GR, Reingold SC. The Multiple Sclerosis Functional Composite Measure (MSFC): an integrated approach to MS clinical outcome assessment. National MS Society Clinical Outcomes Assessment Task Force. *Mult Scler*. 1999;5(4):244-250. doi:10.1177/135245859900500409

128. Monti S, Borrelli P, Tedeschi E, Cocozza S, Palma G. RESUME: Turning an SWI acquisition into a fast qMRI protocol. *PLoS One*. 2017;12(12):e0189933. doi:10.1371/journal.pone.0189933

129. Palma G, Tedeschi E, Borrelli P, et al. A Novel Multiparametric Approach to 3D Quantitative MRI of the Brain. *PLoS One*. 2015;10(8):e0134963. doi:10.1371/journal.pone.0134963

130. Borrelli P, Palma G, Tedeschi E, et al. Improving Signal-to-Noise Ratio in Susceptibility Weighted Imaging: A Novel Multicomponent Non-Local Approach. *PLoS One*. 2015;10(6):e0126835. doi:10.1371/journal.pone.0126835

131. P. Borrelli, G. Palma, M. Comerci, B. Alfano. Unbiased noise

estimation and denoising in parallel magnetic resonance imaging. In: ; 2014:1230-1234. doi:10.1109/ICASSP.2014.6853793

132. Monti S, Pontillo G, Russo C, Cella L, Cocozza S, Palma G. RESUMEN: a flexible class of multi-parameter qMRI protocols. *Physica Medica*. 2021;in press.

133. Draganski B, Ashburner J, Hutton C, et al. Regional specificity of MRI contrast parameter changes in normal ageing revealed by voxel-based quantification (VBQ). *Neuroimage*. 2011;55(4):1423-1434. doi:10.1016/j.neuroimage.2011.01.052

134. Inglese M, Petracca M. MRI in multiple sclerosis: clinical and research update. *Current opinion in neurology*. 2018;31(3):249-255. doi:10.1097/wco.0000000000000559

135. Rooney WD, Johnson G, Li X, et al. Magnetic field and tissue dependencies of human brain longitudinal 1H2O relaxation in vivo. *Magn Reson Med*. 2007;57(2):308-318. doi:10.1002/mrm.21122

136. Allen IV, McKeown SR. A histological, histochemical and biochemical study of the macroscopically normal white matter in multiple sclerosis. *J Neurol Sci*. 1979;41(1):81-91. doi:10.1016/0022-510x(79)90142-4

137. Vrenken H, Rombouts SA, Pouwels PJ, Barkhof F. Voxel-based analysis of quantitative T1 maps demonstrates that multiple sclerosis acts throughout the normal-appearing white matter. *AJNR American journal of neuroradiology*. 2006;27(4):868-874.

138. Yu FF, Chiang FL, Stephens N, et al. Characterization of normal-appearing white matter in multiple sclerosis using quantitative susceptibility mapping in conjunction with diffusion tensor imaging. *Neuroradiology*. 2019;61(1):71-79. doi:10.1007/s00234-018-2137-7

139. Lutti A, Dick F, Sereno MI, Weiskopf N. Using high-resolution quantitative mapping of R1 as an index of cortical myelination. *Neuroimage*. 2014;93 Pt 2:176-188. doi:10.1016/j.neuroimage.2013.06.005

140. Zivadinov R, Tavazzi E, Bergsland N, et al. Brain Iron at Quantitative MRI Is Associated with Disability in Multiple Sclerosis. *Radiology*. 2018;289(2):487-496. doi:10.1148/radiol.2018180136

141. Cocozza S, Petracca M, Mormina E, et al. Cerebellar lobule atrophy and disability in progressive MS. *J Neurol Neurosurg Psychiatry*. 2017;88(12):1065-1072. doi:10.1136/jnnp-2017-316448

142. Benedict RHB, Amato MP, DeLuca J, Geurts JJG. Cognitive impairment in multiple sclerosis: clinical management, MRI, and therapeutic avenues. *The Lancet Neurology*. 2020;19(10):860-871. doi:10.1016/s1474-4422(20)30277-5

Author's Publications

Only publications as one of the main authors, in reverse chronological order:

G Pontillo, et al. *Assessing Neurological Involvement in Fabry Disease with Deep Learning and the Brain-Age Paradigm.* Submitted 2022

G Pontillo, et al. *Neural substrates of verbal memory impairment in schizophrenia: a multimodal connectomics study.* Submitted 2022

G Pontillo, et al. *Stratification of multiple sclerosis patients using unsupervised machine learning: a single-visit MRI-driven approach.* European Radiology 2022

G Pontillo, et al. *Clinical correlates of R1 relaxometry and magnetic susceptibility changes in multiple sclerosis: a multi-parameter quantitative MRI study of brain iron and myelin.* European Radiology 2022

F Barkhof, G Pontillo. *Staying Connected: The Relevance of Motor-specific Transcallosal Fibers.* Radiology 2022

I Gabusi & G Pontillo, et al. *Structural disconnection and functional reorganization in Fabry disease: a multimodal MRI study.* Brain Communications 2022

M Tranfa, G Pontillo, et al. *Quantitative MRI in Multiple Sclerosis: From Theory to Application.* American Journal of Neuroradiology 2022

L Tomasevic, HR Siebner, A Thielscher, F Manganelli, G Pontillo, R Dubbioso. *Relationship between high-frequency activity in the cortical sensory and the motor hand areas, and their myelin content.* Brain Stimulation 2022

M Tranfa, M Tortora, G Pontillo, et al. *The central vein sign helps in differentiating multiple sclerosis from its mimickers: lessons from Fabry disease.* European Radiology 2022

G Pontillo, et al. *A combined radiomics and machine learning approach to overcome the clinicoradiologic paradox in multiple sclerosis.* American Journal of Neuroradiology 2021

S Monti, G Pontillo, et al. *RESUMEN: A flexible class of multi-parameter qMRI protocols.* Physica Medica 2021

M Petracca, G Pontillo, et al. *Neuroimaging correlates of cognitive dysfunction in adults with multiple sclerosis.* Brain Sciences 2021

M Tortora, M Tranfa, AC D'Elia, G Pontillo, et al. *Walk your talk: Real-world adherence to guidelines on the use of MRI in multiple sclerosis.* Diagnostics 2021

G Pontillo, et al. *Unraveling deep gray matter atrophy and iron and myelin changes in multiple sclerosis.* American Journal of Neuroradiology 2021

G Pontillo, et al. *The development of subcortical gray matter atrophy in multiple sclerosis: One size does not fit all.* American Journal of Neuroradiology 2021

G Pontillo, et al. *Diffuse brain connectivity changes in Charcot–Marie–Tooth type 1a patients: a resting-state functional magnetic resonance imaging study.* European Journal of Neurology 2021

C Russo, G Pontillo, et al. *Nonvascular Parkinsonism in Fabry Disease: Results From Magnetic Resonance and Dopamine Transporter Imaging.* Journal of Neuropathology & Experimental Neurology 2021

G Pontillo, et al. *The cerebellum in idiopathic cervical dystonia: A specific pattern of structural abnormalities?* Parkinsonism & related disorders 2020

G Pontillo, et al. *Brain plasticity in Charcot-Marie-Tooth Type 1A patients? A combined structural and diffusion MRI study.* Frontiers in Neurology 2020

L Ugga, G Pontillo, et al. *MRI linear measurements in normal pressure hydrocephalus versus progressive supranuclear palsy.* Movement Disorders 2020

G Pontillo, et al. *2D linear measures of ventricular enlargement may be relevant markers of brain atrophy and long-term disability progression in multiple sclerosis.* European Radiology 2020